Communication in Physical Sciences 2025, 12(5): 1707-1737

Geomechanical Characterization and In-Situ Stresses Analysis for Predicting CO_2 Storage Potential: A Case Study of Toba Field, Niger Delta.

Olowonefa Richard, Auduson, Aaron Enechojo, Ologe Oluwatoyin, Yusuf Odunsanwo, Agbane Isaac Ojodomo

Receieved : 17 April 2025/Accepted : 21 June 2025/Published : 25 June 2025
https://dx.doi.org/10.4314/cps.v12i5.20

Abstract: *This study addresses a critical gap in geological carbon storage (GCS) assessment by explicitly analyzing the brittleness-ductility characteristics and failure mechanisms of caprock-reservoir systems under CO_2 injection-induced stress an area often overlooked in prior research. The mechanical response of subsurface formations whether brittle (leading to fracturing) or ductile (resulting in plastic deformation) directly affects containment integrity, leakage risk, and long-term storage performance. To fill this gap, we conducted a quantitative geomechanical characterization of six wells in the TOBA field, Niger Delta. Results from 1D Mechanical Earth Models (MEMs) show that mechanical strength increases with depth: Young's Modulus rises from 4.95 GPa (shallow caprock) to 9.27 GPa (A6000 reservoir), and UCS increases from 2,427 psi to 4,037 psi. Skerlec's density-based classification identifies hydrocarbon caprocks (2.42 g/cm³) as 37% more brittle than saline equivalents (2.28 g/cm³). Brittleness Index (BI) further confirms this trend, ranging from 0.27 in ductile saline units to 0.39 in the A6000 reservoir. Stress analysis using Mohr-Coulomb criteria shows a transitional failure mode from shear to tensile and that the A6000 hydrocarbon reservoir tolerates the highest pore pressure increment ($\Delta Pp = 21.1$ MPa), while saline reservoirs have the lowest failure threshold ($\Delta Pp = 3.80$ MPa). Stress regime analysis ($Sv > \sigma H > \sigma h$) indicates dominant normal faulting, consistent with Niger Delta growth fault systems. These findings provide critical insights for predicting rock failure behaviour, optimizing injection strategies, and ensuring long-term storage integrity in deltaic settings.*

Keywords: *CO_2 Sequestration, Niger Delta Basin, Mohr-Coulomb failure criterion, Brittleness Index, Fault stability, Geomechanics, 1D MEM*

Olowonefa Richard
Department of Geology, Federal University, Lokoja, Kogi State, Nigeria.
Email: *oloworichardgeo@gmail.com*

Auduson, Aaron Enechojo
Department of Geology, Federal University, Lokoja, Kogi State, Nigeria.
Email: *aaron.auduson@fulokoja.edu.ng*

Ologe Oluwatoyin
Department of Applied Geophysics, Federal University, Birnin Kebbi, Nigeria.
Email: *oluwatoyin.ologe@fubk.edu.ng*

Yusuf Odunsanwo
Dhammatan Oil Nigeria Limited, Lagos State, Nigeria.
Email: *yodusanwo@dharmattangroup.com*

Agbane Isaac Ojodomo
Department of Geology, Federal University, Lokoja, Kogi State, Nigeria.
Email: *isaac.agbane-pgs@fulokoja.edu.ng*

1.0 Introduction

Carbon capture and storage (CCS) is a vital technology for mitigating greenhouse gas emissions and decarbonizing the industrial sector (Metz et al., 2005). It plays a crucial role in achieving global climate targets outlined in international frameworks such as the Paris Agreement (Bui et al., 2018; Boot-Handford et al., 2014). For countries like Nigeria, where the economy heavily depends on oil and gas exports, CCS offers a promising pathway to reduce carbon emissions while sustaining economic growth. Nigeria currently ranks 27th among the world's largest CO_2 emitters, with the energy sector contributing significantly by releasing approximately 209 million metric tonnes of CO_2 equivalent in 2021 (Climate Watch, 2019). The country's geological formations, particularly saline aquifers and depleted hydrocarbon reservoirs, offer promising prospects for long-term CO_2 storage.

The success of geological CO_2 storage is fundamentally linked to the integrity of caprocks and the stability of faults within potential storage formations (Pan et al., 2016; Legentil et al., 2023). However, CO_2 injection perturbs the in-situ stress conditions, potentially reactivating pre-existing faults, compromising caprock integrity, and even triggering induced seismicity (Sun et al., 2023; Raziperchikolaee and Pasumarti, 2020). The concept of fault reactivation, introduced by Sibson (1990), is typically assessed using analytical, semi-analytical, and numerical methods (Nacht et al., 2010). Among these, Mohr diagrams, slip tendency, and dilation tendency analyses are widely adopted to evaluate stress distribution and fault stability. Specifically, Mohr diagrams are effective in visualizing shear and normal stresses acting on faults in three-dimensional space, thus providing insights into faulting mechanisms and reactivation potential (Zoback, 2007; Yin and Ranalli, 1992; Jolly and Sanderson, 1997; McKeagney et al., 2004; Streit and Hillis, 2004).

Geomechanical analysis is essential for evaluating the structural integrity and safety of CCS sites. The Mohr-Coulomb failure criterion, which relies on maximum and minimum principal stresses, is widely used to predict shear failure and provides a conservative estimate of rock strength (Labuz, 2014). A sound understanding of the stress regime and mechanical behaviour of both reservoir and caprock units especially under altered conditions caused by CO_2-rock interactions—is critical to ensuring long-term containment (Kaldi, 2013). This is particularly important for large-scale storage operations, where pressure perturbations may extend over wide areas and intensify the risk of mechanical failure (Zoback, 2010).

A major concern in CCS projects is the potential leakage of injected CO_2 through reactivated faults, natural fractures, or compromised caprocks, which could contaminate freshwater aquifers or lead to surface emissions (Song et al., 2023). The mechanical properties of caprocks especially their shear strength play a crucial role in preventing leakage. For example, mudrocks and shales may exhibit low friction angles, sometimes as low as 10° (Ingram and Urai, 1999; Hajdarwish, 2006). However, ductile caprock formations may deform plastically and self-seal under stress, which can offer superior long-term containment performance compared to brittle, dilatant rocks (Nygård et al., 2006; Ingram and Urai, 1999).

Globally, numerous studies have made substantial progress in identifying suitable geological formations for CO_2 sequestration. Foundational works (Sundquist et al., 2008; Ighalo et al., 2022; Cao et al., 2022) have evaluated options such as depleted hydrocarbon reservoirs, saline formations, and unmineable coal seams. These formations are generally assessed based on porosity, permeability, seal integrity, and storage capacity. Depleted hydrocarbon reservoirs are considered highly suitable due to their well-characterized structures and proven sealing systems, whereas saline formations offer vast capacity but are often limited by geological uncertainties and poorly constrained seals.

In the context of Nigeria's Niger Delta, a region with complex geology and a long history of oil production, several researchers (Umar et al., 2020; Eigbe et al., 2023) have affirmed the region's high potential for geological CO_2 storage. Umar et al. (2020), for instance, applied the CO2CRC (2008) site screening criteria, integrating well log analysis, 3D seismic interpretation, and geomechanical modelling to evaluate storage formations. A key contribution of Umar et al. (2020) study was the determination of a fault reactivation threshold of 3.2 MPa, indicating that significant pore pressure build-up would be required to trigger slip, thus reinforcing the geomechanical stability of the region for long-term CO_2 injection.

Complementing this, Mutadza et al. (2024) and Ojo et al. (2023) explored the mineralogical and geomechanical properties of caprocks using techniques such as X-ray diffraction (XRD), SEM imaging, and triaxial compression testing. Their findings revealed that formations rich in quartz, garnet, and illite exhibit high strength and low reactivity with CO_2, making them promising for containment. These studies underscore the importance of caprock composition and structure in ensuring seal integrity.

However, despite these advances, existing studies have not explicitly assessed the brittleness and ductility characteristics of the caprock and reservoir rocks, nor have they identified the dominant failure mechanisms that might arise under injection-induced stress. This is a critical omission, as the mechanical response of subsurface formations whether brittle, leading to fracturing, or ductile, leading to plastic deformation directly impacts the integrity, leakage risk, and long-term performance of a storage system under the elevated pressure and temperature conditions associated with supercritical CO_2.

Filling this gap will enable more accurate prediction of rock failure behaviour, improve leakage risk assessment, optimize injection strategies, and ensure long-term storage integrity by providing critical insights into how caprock and reservoir formations respond either through brittle fracturing or ductile deformation under the elevated stress and pressure conditions associated with supercritical CO_2 injection.

1.1 Geology of Niger Delta

The Niger Delta Basin is situated along the continental margin of the Gulf of Guinea in equatorial West Africa, positioned between latitudes 4°N and 7°N and longitudes 3°E and 9°E (Whiteman, 1982; Abiola and Obasuyi, 2020; Osokpor and Maju-Oyovwikowhe, 2021). The basin originated from a rift triple junction that led to the formation of the South Atlantic Ocean, starting in the late Jurassic and extending into the Cretaceous. Onshore, it lies within the geological context of southern Nigeria and southwestern Cameroon. The northern boundary is marked by the Benin Flank, a hinge line running east-northeast and south of the West African basement massif (Nwachukwu and Chukwurah, 1980).

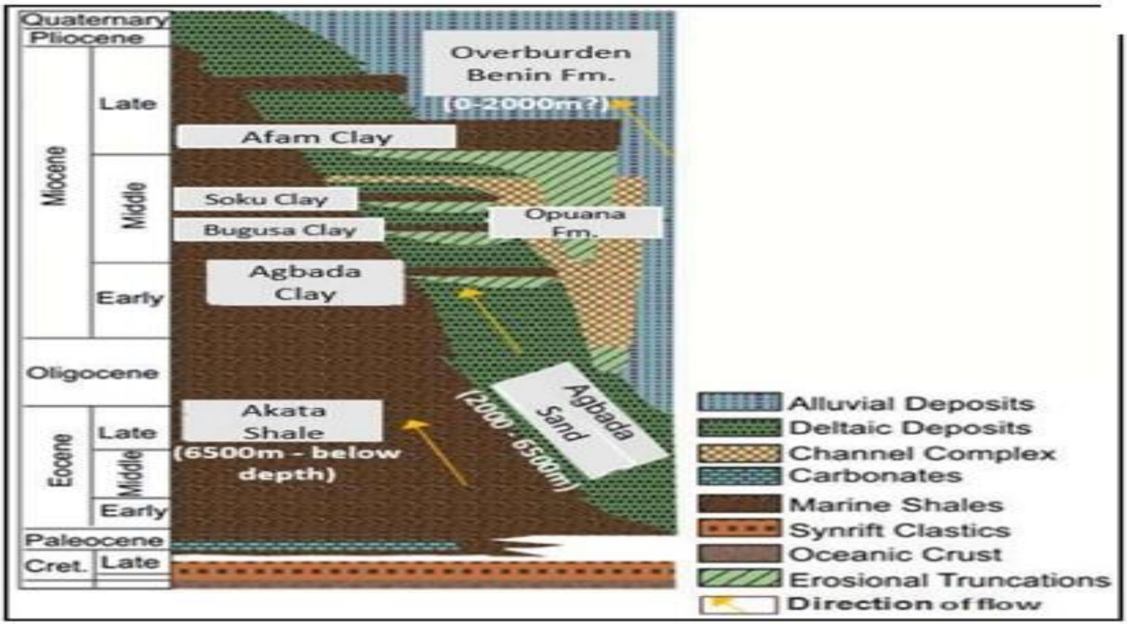

Fig. 1. (a) Stratigraphic sequence in the Niger Delta basin modified after (Folorunso et al., 2015)

Notably, three formations, Akata, Agbada and Benin formation are widely recognized for representing portions of the tripartite sequence, often Agbada formation is characterized by varying sand and shale content (Short and Stäuble, 1967; Avbovbo, 1978).

The Akata Formation forms the foundational layer of the Niger Delta's sedimentary structure. It primarily consists of dark gray shale, with occasional sandy and silty zones. Traces of plant remains and mica are sometimes observed in its upper sections. Rich in micro-fauna, the Akata Formation is regarded as the primary source rock for oil and gas in the Niger Delta, with planktonic foraminifera indicating that the sediments were deposited on a shallow marine shelf. This formation, about 7,000 meters thick in central parts of the delta, dates from the Paleocene to the Holocene and is generally located beneath diapirs and high-pressure zones, often exhibiting overpressure (Doust and Omatsola, 1990).

Above the Akata Formation lies the Agbada Formation, characterized by alternating sand and shale layers of varying thickness, representing the delta's cyclic sedimentary sequences. This unit, rich in fossils that serve as source rocks, comprises deltaic deposits in environments ranging from delta-front to delta-topset and fluvial-deltaic zones (Ekweozor and Okoye, 1980; Nwachukwu and Chukwurah, 1986). This alternation of fine and coarse materials forms multiple reservoir-seal systems, with sequences found in each depobelt, ranging in age from the Eocene to the Pleistocene. The Agbada Formation, over 3,700 meters thick, represents the main deltaic sequence.

The uppermost layer, the Benin Formation, consists largely of freshwater fluvial sands and some gravels, interspersed with shale beds at its base. Benin sands are poorly sorted, ranging from fine to coarse grains, and vary from sub-angular to well-rounded, often appearing white to yellowish-brown. These sands and gravels were deposited by graded channels as point bars, with finer sediments laid down in back-swamps and lakes. The oldest sands in this formation may date back to the Oligocene, though they lack fauna, making precise dating difficult. Offshore, the formation thins and disappears near the shelf edge. While these three formations are formally distinguished, they primarily differ in their sand-to-shale ratios (Short and Stäuble, 1967).

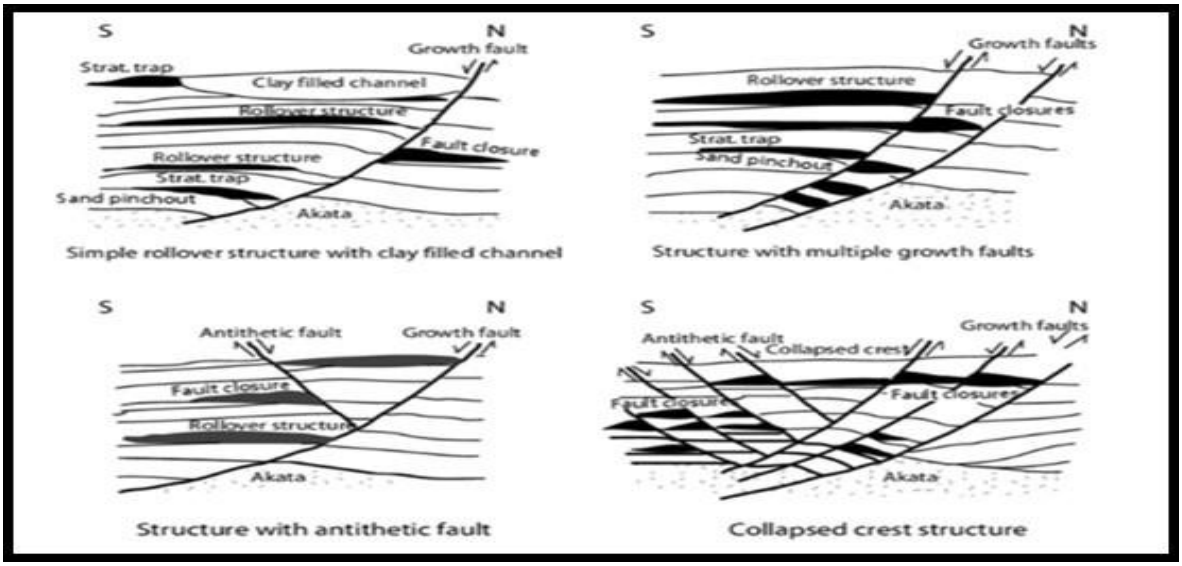

Fig. 2. Structural style of the extensional area of the Niger Delta (Doust and Omatsola, 1990)

In the Niger Delta fields, most known hydrocarbon traps are structural, although stratigraphic traps are also present. The structural traps formed as a result of synsedimentary deformation within the Agbada paralic sequence (Obasuyi et al., 2019). Structural trapping mechanisms in the region include a range of features, such as simple rollover structures, clay-filled channels, growth fault complexes, antithetic faulted structures, and collapsed crest structures. Normal faults are caused by extensional tectonic regime. Growth faults are synsedimentary normal fault. The vertical offsets of these faults increases with depth. These types of faults are mostly characterized with the Niger Delta reservoirs (Auduson, 2018).

1.3 Location of Study Area

The study area is TOBA-field onshore part of the Niger Delta. The field was discovered by drilling of TOBA-01. Till date 6 wells have been drilled. Fig. 1.5.below show map of Nigeria and onshore part of the depobelt where TOBA-field is located and the 6 wells in TOBA-field.

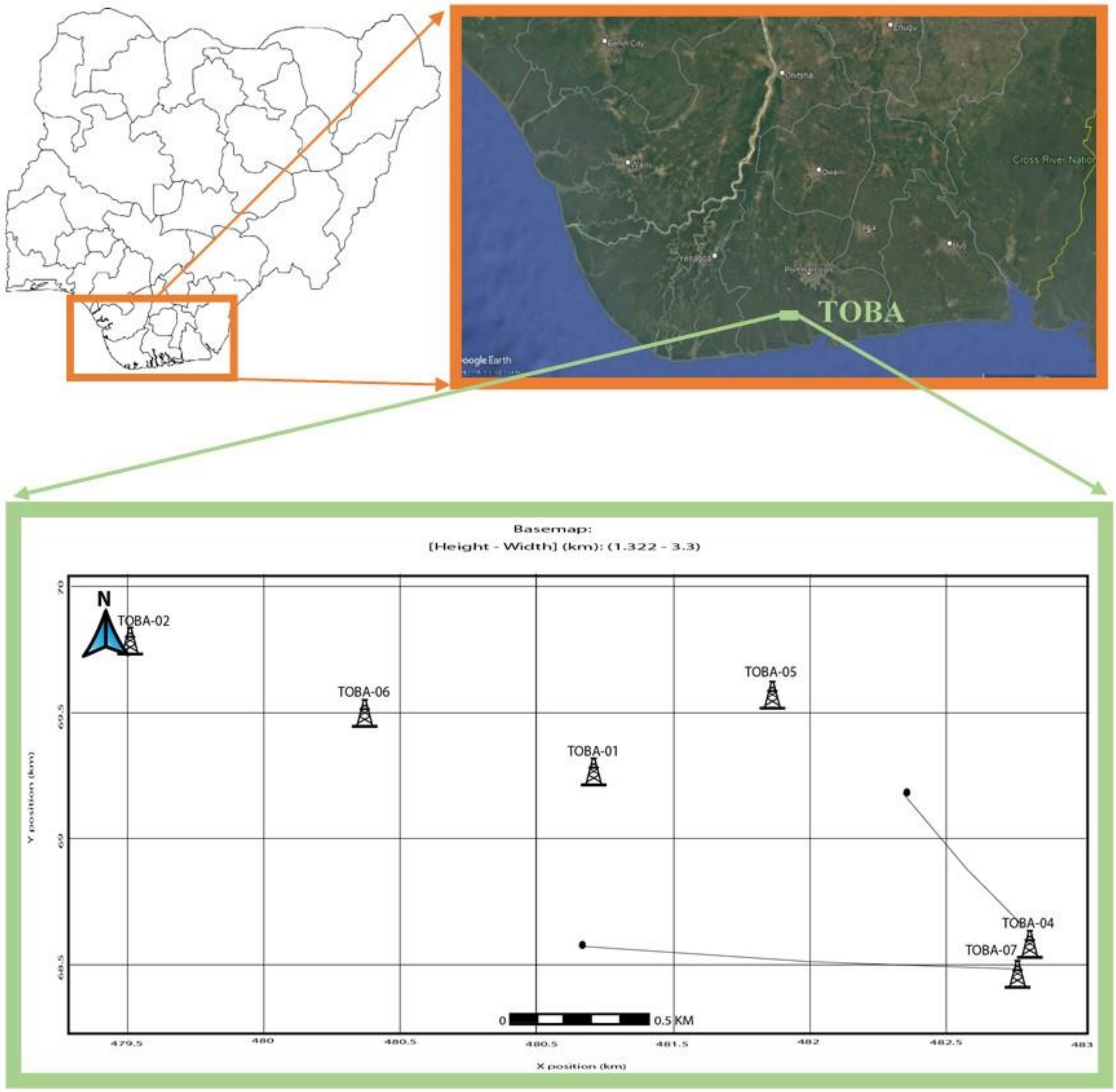

Fig. 3. Map showing location of TOBA-field in Niger Delta, Nigeri

2.0 Materials and Methods

2.1 Materials

The materials used for this study include; Well data in las format for six wells (TOBA-01, TOBA-02, TOBA-04, TOBA-05, TOBA-06 and TOBA-07), deviation survey and Checkshot data from a multinational oil company. The well logs with their depth of penetration is seen Table 1. After quality check of well log data using histogram plot Techlog, only Wells TOBA-05 have the basic log suite for the analysis. For this study, Microsoft Excel, Mohr Plotter by Richard Allmendinger, Schlumberger's Petrel and Techlog software was used for all the analysis and interpretations.

Table 1. Available well logs and depth of availability

Measurement Type	TOBA-01	TOBA-02	TOBA-04	TOBA-05	TOBA-06	TOBA-07
Gamma Start (ft)	451.07	499.84	6880.20	10492.90	3917.63	2800.09
Gamma Stop (ft)	12443.90	11649.30	12100.70	11375.70	11673.80	13088.20
Resistivity Start (ft)	490.60	510.29	6880.20	10492.90	3917.63	2800.09
Resistivity Stop (ft)	12443.90	11649.30	12100.70	11375.70	11673.80	13088.20
Density Start (ft)	—	—	11065.50	10492.90	3938.16	2800.09
Density Stop (ft)	—	—	12076.90	11375.70	11638.40	13088.20
Neutron Start (ft)	—	—	11065.50	10492.90	3938.16	2852.75
Neutron Stop (ft)	—	—	12076.90	11375.70	11666.20	13088.20
Sonic Start (ft)	—	461.16	52.22	10492.90	3917.63	—
Sonic Stop (ft)	—	12995.10	13000.70	11375.70	11673.80	—

This study employs a well log-driven workflow that integrates multiple geomechanical and rock property analyses to evaluate CO_2 storage suitability. The process involves the use of well log data for deriving petrophysical parameters and constructing a 1D Mechanical Earth Model (MEM). Brittleness index analysis and Skerlec's model are applied to characterise the mechanical behaviour of both reservoir and caprock units. The workflow also incorporates 3D Mohr stress analysis to assess failure potential in intact rocks and fault planes. This comprehensive approach supports the evaluation of storage integrity and injection safety. The workflow is illustrated in the Fig. 4 below.

2.2 Methods

2.2.1 Well correlation

A correlation is a hypothesis that units in two separated sequences are equivalent (Barros and Andrade, 2009). Correlation of rock units in TOBA field was done with gamma log for lithology delineation and deep resistivity log for fluid type identification.

2.2.2 Estimation of Shear Wave Velocity from Compressional Sonic Data

Most of such estimates have been based on published empirical relations (Castagna et al., 1985).

V_p known as compressional wave velocity was used to estimate V_p from the compressional wave sonic transit time log (DTc).

$$V_p = (1000/DTc)*0.305 \text{ (km/s)} \qquad (1)$$

Shear wave velocity (V_s) was estimated from V_p using the following empirical relationships using Castagna equation (Castagna et al., 1993).

$$V_s = (0.804*V_p) - 0.856 \text{ (km/s) For sandstones} \qquad (2)$$

$$V_s = (0.7700 * V_p) - 0.8674 \text{(km/s) For shales} \qquad (3)$$

$$DTs = 305/ V_s \text{ (µs/ft)} \qquad (4)$$

Where DTC is compressional slowness (µsec/ft), DTs is shear slowness (µsec/ft), V_p is compressional velocity (km/s) and V_s is shear velocity (km/s).

2.2.3 Synthetic Density

Extrapolation method was used to estimate the density of unavailable surface part of the density log.

$$\rho_{extrapolated} = \rho_{mudline} + A_0 *(TVD - AirGap - WaterDepth)^{\alpha} \qquad (5)$$

Where $\rho_{mudline}$ is the density at the sea floor or ground level, A_0 and α are the fitting parameters.

When a synthetic density is created and combined with measured bulk density, the last step is a simple integration of this density curve that starts at depth of zero.

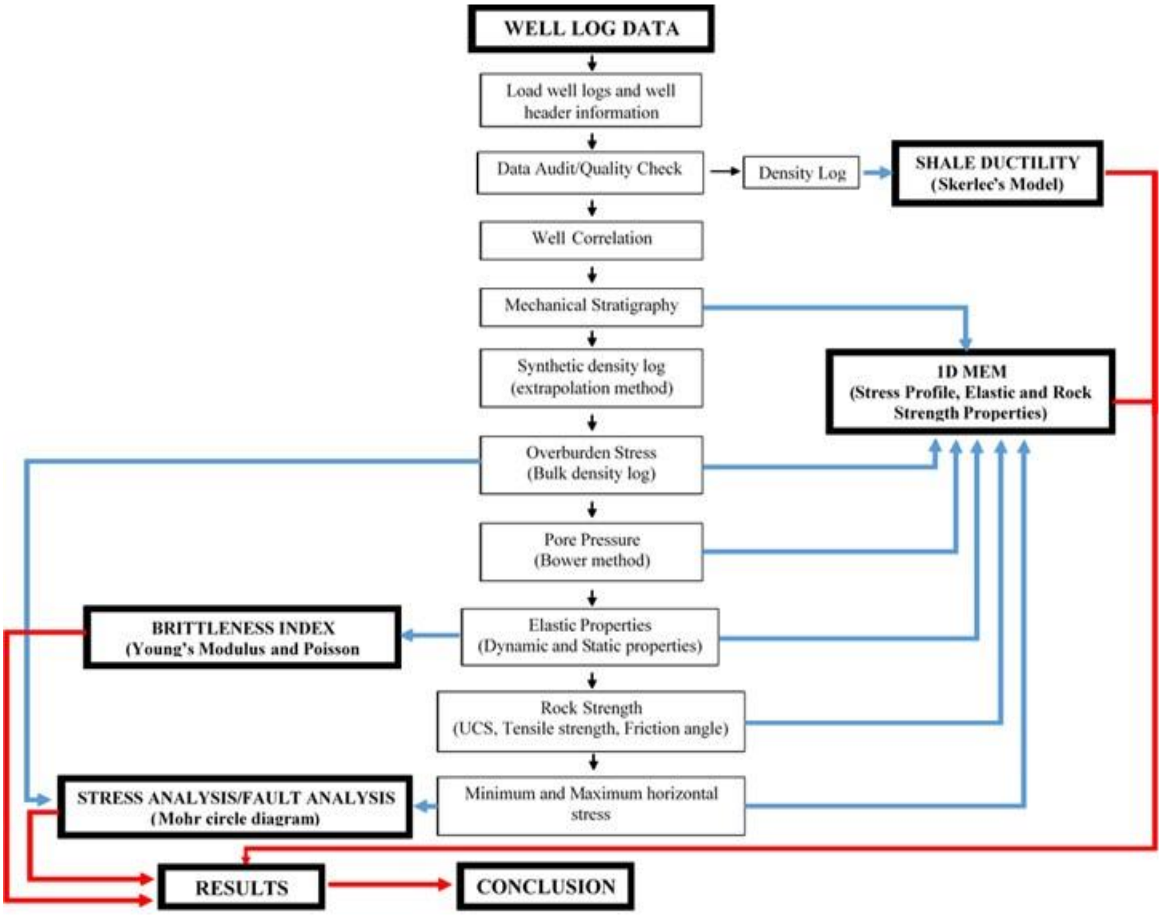

Fig. 4. Research Workflow

2.2.4 *Overburden Stress (σv)*

Overb;urden stress or vertical stress is defined as the pressure exerted on a material at a given depth due to the total mass of the rocks and/or fluids above it (Aird, 2019). The overburden stress is calculated from the bulk density as follows:

$$\sigma_v = g \int_0^{TVD} p_b(z)dz \qquad (6)$$

where σ_v is the vertical stress or overburden stress at depth *TVD*, ρ_b is the bulk density (including the water section above sea floor) and g is the gravitational constant.

Vertical Stress and Terzaghi's Law: The vertical effective stress is defined using Terzaghi's law expressed as equation 7

$$\sigma_v' = \sigma_v - P_p \qquad (7)$$

2.2.5 *Pore Pressure (Pp)*

The Bowers method was initially developed by G.L. Bowers (Bowers, 1995). However the modified bowers method was used in equation 8 given below,

$$\sigma_v' = \sigma_{ref}' \times \left[\frac{V - V_0}{V_{ref} - V_0}\right] \qquad (8)$$

where V is compressional velocity (or the reciprocal of slowness), V_o is velocity in at zero effective stress, V_{ef} is the reference velocity inputted by the user and σ'_{ref} is the effective stress reference of rock when its velocity reaches V_{ef}. β is the velocity exponent.

2.2.6 Dynamic Elastic Properties

Given the assumption of a homogeneous, isotropic, and elastic formation, dynamic shear and bulk modulus, G_{dyn} and K_{dyn}, was be computed means of the following equations (Fjaer et al., 2008)

$$G_{dyn} = (13474.45)\frac{p_b}{(\Delta t_{shear})^2} \qquad (9)$$

$$k_{dyn} = (1347.45)p_b \left[\frac{1}{(\Delta t_{shear})^2}\right] - \frac{4}{3} G_{dyn} \qquad (10)$$

where: ρ_b is bulk density of the formation (g/cm^3), Δt_{comp} is compressional slowness of the bulk formation us/ft and Δt_{shear} is shear slowness of the bulk formation us/ft.

Dynamic Young's Modulus (E_{dyn}), Poisson ratio (v_{dyn}), Shear (G_{dyn}) and Bulk (K_{dyn}) modulus where computed using the equations below as following (Zoback, 2007)

$$E_{dyn} = \frac{9G_{dyn} - k_{dyn}}{G_{dyn} + 3k_{dyn}} \qquad (11)$$

$$v_{dyn} = \frac{3k_{dyn} - 2G_{dyn}}{G_{dyn} - 3k_{dyn}} \qquad (12)$$

$$v_{dyn} = \frac{R_{sp}^2 - 2}{2R_{sp}^2 - 2} \qquad (13)$$

$$R_{sp} = \frac{\Delta t_{shear}^2}{\Delta t_{comp}^2} \qquad (14)$$

where R_{sp} is the ratio of shear and compressional slowness.

2.2.6 Elastic Properties

All elastic properties of materials are interrelated and can be mathematically derived if the preferable data is not available (Mavko et al., 2020). Mathematical relationships can be used to derive certain properties if others are known, or calculated using other means such as sonic data from well logs.

Young's Modulus: Modified Morales correlation which was developed in 1997 was used to estmaite static Youngs' Modulus below.

$$E_{st} = (-2.21PHIT_{ND} + 0.965)E_{dyn} \qquad (15)$$

where $PHIT_{ND}$ is total porosity and E_{dyn} is the dynamic Young's Modulus

Poisson's Ratio: Poisson's ratio expresses the relationship between transverse strain to axial strain or the deformation of a material (Słota-Valim, 2015).

$$V_{st} = V_{dyn} * PR\ multiplier \qquad (16)$$

PR multiplier is unitless. The default value of *PR multiplier* is 1.0, then the static Poisson ratio is equal to the dynamic Poisson ratio.\

Shear modulus: The shear modulus \expresses the ratio of shear stress to shear strain (Archer and Rasouli, 2012). Static shear modulus was computed using the following equation

$$G_{sta} = \frac{E_{sta}}{2(1 + v_{sta})} \qquad (17)$$

Bulk modulus: Bulk modulus was computed using the equation 18,

$$k_{sta} = \frac{E_{sta}}{3(1 - 2v_{sta})} \qquad \mathbf{(18)}$$

Biot's Coefficient: Mecpro Alpha Model estimates Biot's Coefficient by assuming that the skeleton (dry) Bulk Modulus is equal to the Bulk Modulus.

$$\alpha = 1 - \frac{k_{skeleton}}{k_{solid}} \qquad (19)$$

$$\alpha = 1 - \frac{k_{bulk}}{k_{solid}} \qquad (20)$$

where K_{bulk} = Static Bulk Modulus, K_{solid} = Static solid bulk Modulus and $S_{keleton}$ is used in model only for derivation and not for calculation.

2.2.8 Rock Strength

Unconfined compressive strength (*UCS*): The Coates-Denoo algorithm introduced in the late 1960's was used to compute the unconfined compressive strength.

$$\boldsymbol{C_0} = 0.0866 \times \frac{E_{dyn}}{Cdyn}(0.008v_{sh} + 0.0045(1 - V_{sh})) \qquad (21)$$

where C_{dyn} is the Dynamic Bulk Compressibility, can be expressed as,

$$C_{dyn} = \frac{1}{k_{dyn}} \qquad (22)$$

with, C_o = Unconfined Compressive Strength (Mpsi), E_{dyn} = Dynamic Young's Modulus (Mpsi), K_{dyn} = Dynamic Bulk Modulus (Mpsi) and V_{sh} = Volume of Clay type material Relative to total volume.

Friction Angle: Friction Angle (ϕ) was computed from GR log. An empirical correlation to determine friction angle was used Kadyrov (2012) and found in the work by Albukhari et al. (2018). This method maps Gamma Ray to Friction Angle with a linear correlation.

Cohesion: Cohesion is one of the parameters used in the Mohr-Coulomb failure criterion, which describes how materials fail under different stress conditions. Cohesion as a function of UCS and friction angle was used to compute cohesion as proposed by Jaeger (2009).

$$COH = \frac{UCS}{2\left\lfloor\sqrt{1 + (tanFANG)^2 + tanFANG}\right\rfloor} \qquad (23)$$

where UCS = Unconfined Compressive Strength and $FANG$ = Friction angle

Tensile Strength: Tensile strength as a function of UCS model provides the simple correlation to compute tensile strength directly from UCS strength.

TSTR = K * UCS (24)

Where K = Facies and zone based factor (default = 0.1). This default value is based on the Griffith Elastic-brittle theory which gives the ratio of compressive strength versus tensile strength for 8 ~ 12.

2.2.9 Horizontal Stresses

Minimum Horizontal stress: Mohr-Coulomb Stress Model is a failure model that gives a relationship between two principal stresses if the formation is at failure was used to estimate the horizontal stress.

$$\sigma_h = \frac{(\sigma_v - \alpha P_p)}{tan^2\left(\frac{\pi}{4}+\frac{\theta}{2}\right)} \qquad (25)$$

where σ_v = Total Vertical Stress, P_p = Pressure of the fluids or gases occupying the pore space (voids or holes) in the rock at a particular depth of interest, θ = Friction Angle and α = Biot's Coefficient

Maximum Horizontal stress: Maximum horizontal stress is the largest principal stress in the horizontal plane. The maximum horizontal stress along with the minimum horizontal stress, defines the stress state of the rock and influences the direction in which fractures are likely to propagate.

$$\sigma_H = \sigma_h * Multiplier \qquad (26)$$

The multiplier applied to minimum horizontal stress to get the maximum horizontal stress. The default value is 1.1.

2.2.10 Brittleness Index

Grieser and Bray (2007), expressed the term average brittleness as an empirical relationship between Poisson's ratio and Young's modulus to distinguish ductile from the brittle area as determined by the equation:

$$E_{brittleness} = \frac{E - E_{min}}{E_{max} - E_{min}} \qquad (27)$$

$$v_{brittleness} = \frac{v - v_{max}}{E_{min} - E_{max}} \qquad (28)$$

$$B_{avg} = \frac{E_{brittleness} + v_{brittleness}}{2} \qquad (29)$$

where, E_{max} = maximum value of Young's Modulus, E_{min} = minimum value of Young's Modulus, υ_{max} = maximum value of Poisons ratio, υ_{min} = minimum value of Poisons ratio and B_{avg} =Average of the sum of $E_{brittleness}$ and $\upsilon_{brittleness}$.

Table 2. Relationship between brittleness index and brittleness of rock modified from (Rojas et al., 2016, June and Yang et al., 2013)

Brittleness index	Nature of rock in terms of brittleness
0-0.16	Ductile
0.16-0.32	Less ductile
0.32-0.48	Less brittle
Greater than 0.48	Brittle

2.2.11 Skerlec Model for Ductility of Shale (Caprock)

Hoshino et al (1972), Boggs (1995) and Skerlec (1982) agreed that there is a relationship between depth and density in terms of the ductile and brittle nature of shale. According to Hoshino and his team, mudrock (shale) densities less than 2.2 g/cm^3 show ductile behaviour, mudrocks with 2.2-2.5g/cm^3 are transitional and expected to show a wider range of mechanical behaviour and mudrocks with densities higher than 2.5g/cm^3 are expected to show brittle behaviour.

2.2.12 Anderson Fault Regime Classification Scheme

The Anderson model is a pivotal theory in structural geology, offering a foundational approach to understanding brittle fracture in rocks as first outlined by Jaeger and Cook (1979). Over years of development, the Anderson model has become essential in fault mechanics.

Works of Anderson (1951) and Cerveny et al. (2004) agree that when rocks fail in shear, three distinct stress regimes emerge. These regimes correspond to Anderson’s classifications of fault types, a system widely adopted to describe the fundamentals of fault orientation and failure. Here, the stress state is defined by three perpendicular principal stresses: the maximum, intermediate, and minimum stresses σ1 > σ2 > σ3 (Twiss and Moores, 1992). In this model, the lithostatic load typically acts vertically, while the two horizontal stresses orient orthogonally (Cerveny et al., 2004; Economides and Nolte, 2000).

According to Anderson’s classifications, a normal fault has a dip of 60°, a thrust fault has a dip of 30°, and a strike-slip fault forms at a dip of 30° (Twiss and Moores, 1992). Anderson’s model assumes that in normal faulting, the maximum principal stress (overburden) is vertical; in thrust faulting, the minimum horizontal stress is vertical; and in strike-slip faulting, the intermediate horizontal stress is vertical (Zoback, 2007).

2.2.13 Mohr Circe (Stress and Fault Analysis)

The shear stress τ is the stress component, which acts along the fracture plane. It is written using the principal stress components as follows in equation 30:

$$\tau = c + \sigma'_n tan\phi \qquad (30)$$

The cohesional failure envelope is used for rocks that have a cohesional and tensile strength. The cohesionless failure envelope is used for granular materials (soils and unconsolidated sediments with no cohesion or tensile strength, or for rocks that contain cohesionless fractures (Sibson, 2000).

The faults, pre-existing fractures and failure of soils are often assumed to be cohesionless and the friction coefficient is typically in the range of μ = 0.6–0.85 (Byerlee, 1978 ; Sibson, 1985). Lower friction values are found in faults that contain clay minerals (Streit and Hillis, 2002). Assessments of fault stability require knowledge of fault geometries.

Where τ is shear stress of shear plane, σ'_n is the effective normal stress, c is the cohesion of rock, and ϕ is the frictional angle of rock. These effective normal stress and shear stress are obtained from the Mohr circle, which in equation form is (Jaeger and Zimmerman, 2009)

$$\sigma'_n = \frac{(\sigma_1+\sigma_3)}{2} + \frac{(\sigma_1-\sigma_3)}{2} cos2\phi \qquad (31)$$

$$\tau = \frac{(\sigma_1-\sigma_3)}{2} sin2\theta \qquad (32)$$

where σ_1 is the maximum principal stress and σ_3 is the minimum principal stress while σ'_1 and σ'_3 are maximum and minimum effective stress. Shear failure can be represented graphically as the intersection of the Mohr circle with the Coulomb criterion. There are two primary shear failure mechanisms during geological CO_2 storage are intact rock shear failure and fault reactivation.

The ratio of shear to normal stress acting on the surface is the slip tendency (T_S) and is defined mathematically in equation 33 as follows:

$$T_s = {}^{\tau}\!/_{\sigma'_n} \qquad (33)$$

In this equation above, τ is the shear stress, and σ'_n is the effective normal stress ($\sigma_n - P_f$). According to Rutqvist et al. (2007), for a cohesionless fault, the slip will occur when the following condition in equation 34 is met:

$${}^{\tau}\!/_{\sigma'_n} \geq \mu_s \qquad (34)$$

where μs is the static frictional coefficient.

Dilation tendency analysis, first introduced by Ferrill et al. (1999), investigates the ability of a fault to act as a fluid conduit by reactivation in the current stress field or intact rock to undergo tensile failure into the cap rock (hydraulic fracturing) (Kulikowski et al. 2016). The normal stress can be normalized by the differential stress to give the dilation tendency (Moeck et al. 2009). Dilation tendency is calculated using the following equation 35 below:

$$T_d = \frac{\sigma'_1 - \sigma'_n}{\sigma'_1 - \sigma'_3} \qquad (35)$$

where T_d is dilation tendency, σ'_1 is the maximum effective principal stress, σ'_3 is the minimum effective principal stress, and σ'_n is the effective normal stress acting on the fault plane. This relationship shows that as σ'_n approaches σ'_3, the tendency of the fault plane to dilate increases and remains open to potential fluid flow. The fault will have a higher dilation tendency as T_d approaches one. T_d values range from 1 (one), a fault plane that is ideally oriented to slip or dilate under current stress field to 0 (zero), a fault plane with no potential to slip or dilate.

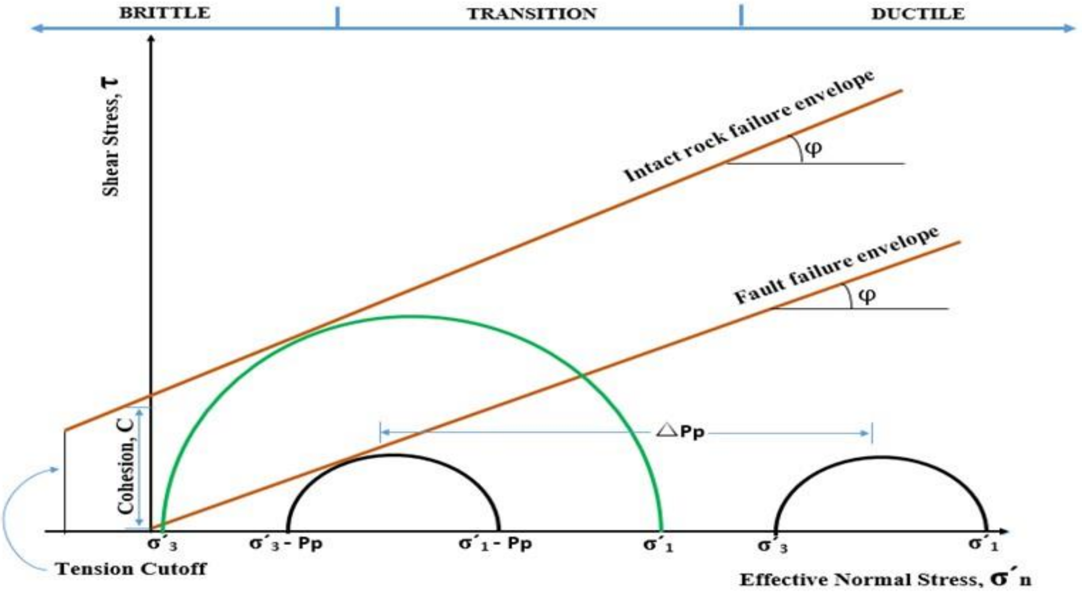

Fig. 5. **Failure envelope diagram illustrating brittle-ductile transition under shear stress and effective normal stress *(adapted from Lee et al., 2017; Nygård et al., 2006)***

3.0 Result and Discussion

3.1 Well Correlation

The six (6) wells in TOBA field (TOBA-02, TOBA-06, TOBA-01, TOBA-05, TOBA-04 and TOBA-07) were correlated and 6 reservoir sandstones were identified, sand A3000 (saline formation) and A6000 (hydrocarbon reservoir) were chosen as reservoirs of interest. Gamma and resistivity log was used for the correlation of the well in TOBA field. Stratigraphic correlation of the wells in TOBA field revealed continuity of the lithological units as seen in Fig. 9.

The correlated wells in TOBA field (Fig. 6) using gamma and resistivity log showed that the rock units are continuous except in well TOBA-06 where sand A5000 is missing but continues in well TOBA-02 which is likely that TOBA-06 penetrated through one of the fault plane. The correlation also revealed the geology of TOBA field in consonance with that mentioned by Short and Stäuble (1965); Avbovbo (1978).

The youngest rock formation is the Benin formation with low gamma ray reading and high resistivity reading, indicative of fluvial sands with fresh water as the fluid it contains. The Benin on the gamma ray logs of the wells in TOBA-field start from a height of 500ft to approximately 7850ft. The Agbada formation which is overlain by the Benin start at depth of approximately 7850ft to a depth of approximately 11200ft characterized by varying reading of gamma indicative of alternation of rock type between sandstone and shale. The sandstones in the Agbada formation serve as the reservoir and the shale serve as the caprock. The lower portion of the Agbada is seen with high resistivity reading indicative of hydrocarbon compared to the uppermost part of the Agbada formation which could have been as a result of migration of hydrocarbon not been able to get to those part from the source rock below. The Akata formation which is overlain by the Agbada formation is characterized with very high gamma log reading indicative of shale which is the source rock of the Agbada-Akata Petroleum system. The Akata formation of TOBA-field was not penetrated by any of the wells.

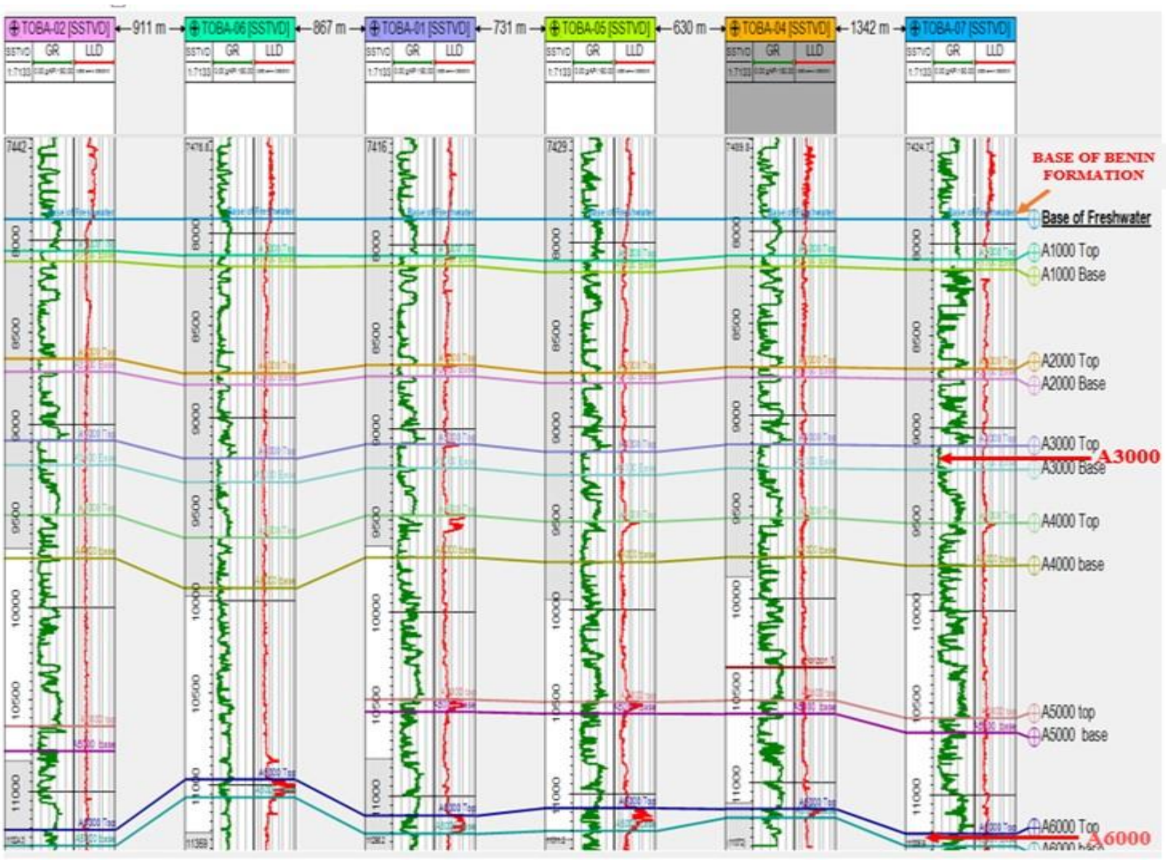

Fig. 6. Stratigraphic correlation of the six wells in TOBA field

\3.2 *Estimation of Vertical Stress*

The one dimensional mechanical earth model was built first with estimation of density which is important for the production of vertical stress. The extrapolation method was used and the result is shown below in Fig. 7 for TOBA-05. Fig. 7 present the profile for the Synthetic, Extrapolated Density, Overburden Mud Weight and overburden pressure (Vertical pressure) for TOBA-05).

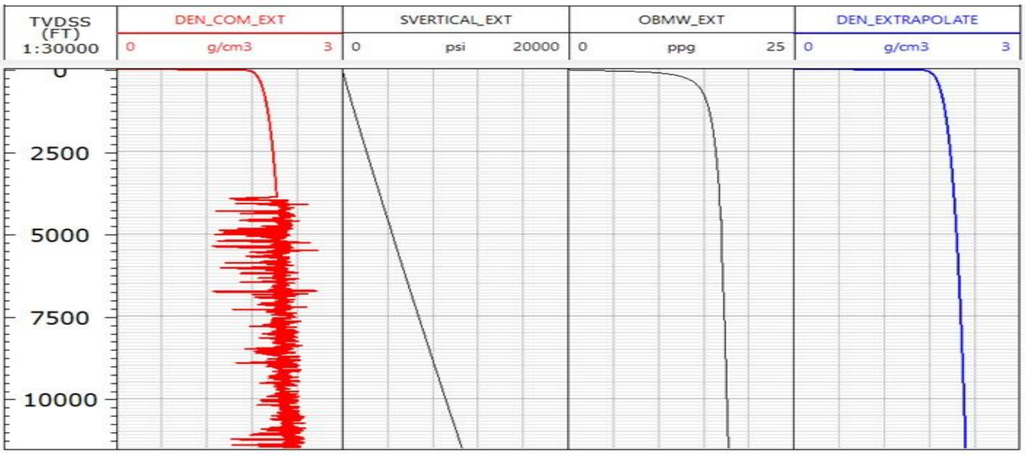

Fig. 7. Synthetic, Extrapolated Density, Overburden Mud Weight and overburden pressure (Vertical pressure) Profiles for TOBA-05

The red curve represent the measured/computed density (DEN_COM_EXT), while the blue curve represents the extrapolated density (DEN_EXTRAPOLATE). In the plot, the density begins to stabilize with depth, reflecting compaction-related increases in density due to overburden pressure. The extrapolated density curve aligns closely with the computed/measured density, indicating consistency in the data.

The extrapolation account for regions where direct data measurements are unavailable. The black curve (VERTICAL_EXT) represents the estimated overburden pressure as a function of depth. This parameter is crucial in geomechanics, as it reflects the cumulative weight of the overlying rock and fluid columns. The overburden pressure increases linearly with depth, as expected, due to the accumulation of rock and sediment mass. The OBMW_EXT (Equivalent Mud Weight) curve represents the required mud weight (in pounds per gallon, ppg) to balance the overburden pressure at any given depth. This parameter is derived from the vertical stress (overburden pressure), calculated using the extrapolated density profile. The OBMW_EXT curve increases with depth, as expected, because the overburden pressure accumulates with the weight of overlying rock and fluids. The curve appears smooth and follows a near-linear trend, consistent with typical compaction and overburden stress in sedimentary basins.

3.3 Elastic static and dynamic properties

The elastic properties of TOBA-05 was also estimated and the logs generated are seen below in Fig. 8 plotted in five tracks each containing both static and dynamic elastic property of the well.

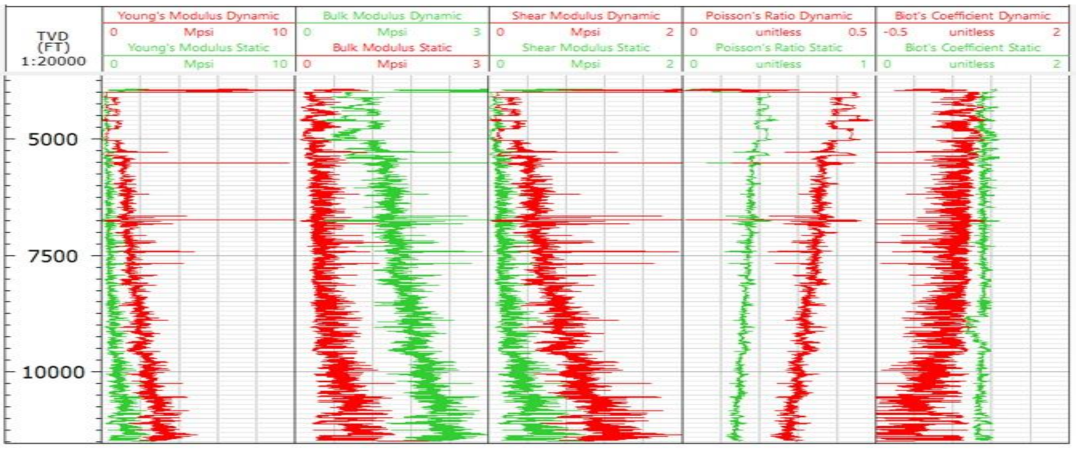

Fig. 8. Dynamic and Static Elastic Moduli of well TOBA-05

The elastic properties of well TOBA-05 were evaluated and the logs of these properties generated is seen in Fig. 8. These elastic properties are Young's Modulus, Bulk Modulus, Shear modulus and Poisson ratio. Dynamic Young's Modulus (red curve) measures the elastic stiffness of the rock under high-frequency dynamic loading, derived from acoustic velocity measurements while the Static Young's Modulus (green curve) reflects the rock's stiffness under slow, in-situ stress conditions. Variability in the modulus values suggests changes in rock stiffness with depth, indicative of lithological heterogeneity. Higher values of Young's modulus often correlate with more competent, consolidated formations sandstones, whereas lower values likely represent less compacted or more porous formations shales. Dynamic Bulk Modulus (red curve) represents rock compressibility under uniform pressure loading in dynamic conditions. Static Bulk Modulus (green curve): Indicates compressibility under slower, quasi-static conditions. Variability in bulk modulus suggests that compressibility changes with lithology and porosity. Lower bulk modulus intervals may indicate zones of higher porosity or less compacted sediments. Lower bulk modulus intervals may point to higher porosity, potentially correlating with better reservoir quality. The Shear Modulus measures the rock's ability to resist deformation under shear stress. Variations in shear modulus reflect changes in rock strength and ductility. Higher shear modulus values are likely associated with more rigid formations like sandstone while lower values indicate softer formations shales, which may be more prone to shear deformation or failure under stress. Poisson's Ratio describes the relationship between lateral and axial strain when a rock is subjected to stress. Dynamic Poisson's Ratio (red curve) is slightly higher than the static counterpart (green curve), as dynamic measurements often neglect inelastic strain components. Poisson's Values generally range between 0.2 and 0.4, which are typical for sedimentary rocks. Variability in Poisson's Ratio indicates changes in the rock's ductility and brittleness. Higher values suggest ductile formations, while lower values point to brittle behaviour.

Generally, Young Modulus, Bulk Modulus and Shear Modulus all increases with depth in well TOBA-05 because increase in overburden leads to a decrease in porosity and thus formation compaction as seen in Fig. 8.

3.4 1D MEM

The 1D MEM that consist of the Mechanical stratigraphy, Poisson ratio, Young's Modulus, frictional angle, cohesion, Tensile strength, UCS (Unconfined Compressive Strength), Pore pressure, Vertical stress (overburden stress), Maximum and Minimum horizontal stress. The different tracks that make up the 1D MEM are seen below for TOBA-05.

The 1D Mechanical Earth Model (MEM) result presented in Fig. 9 represents the geomechanical characterisation of the caprock (shale) overlying the saline formation (sandstone). This figure provides insights into the variation of elastic and strength properties with depth within the saline formation.

In contrast, Fig. 10 displays the 1D MEM result for the caprock (shale) and the underlying hydrocarbon reservoir (sandstone), allowing for a comparative evaluation of geomechanical behaviour across the two distinct storage formations.

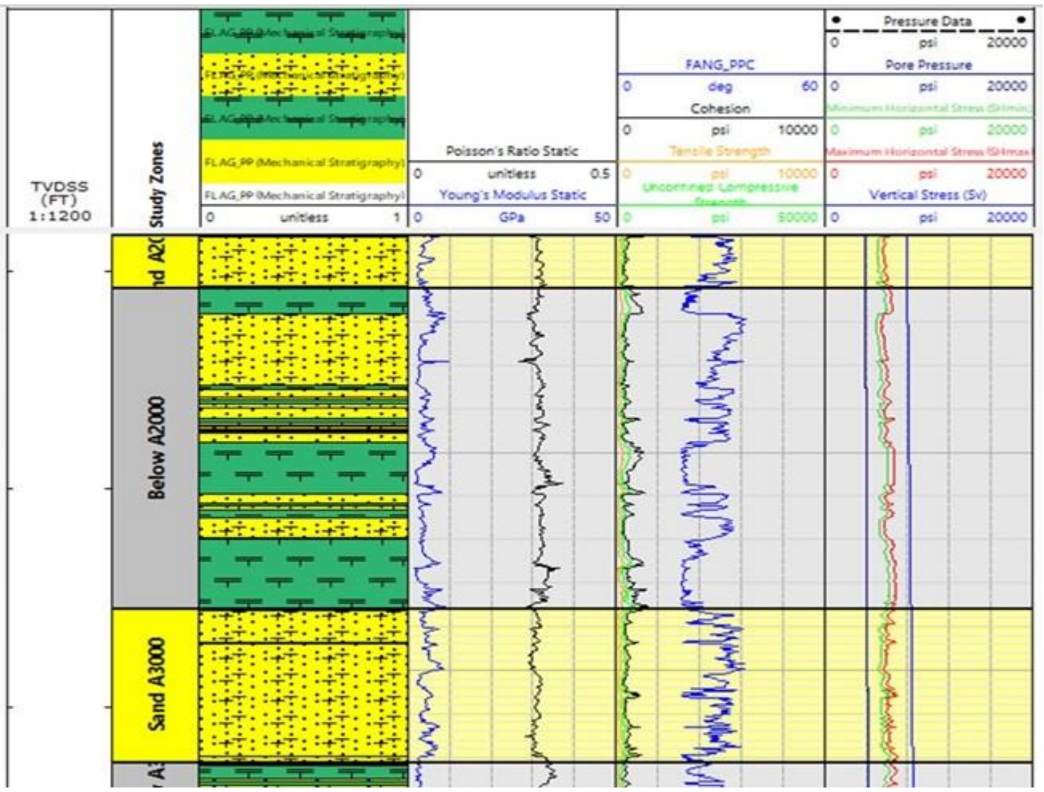

Fig. 9. 1D MEM of well TOBA-05 for zone below A2000 and Sand A3000

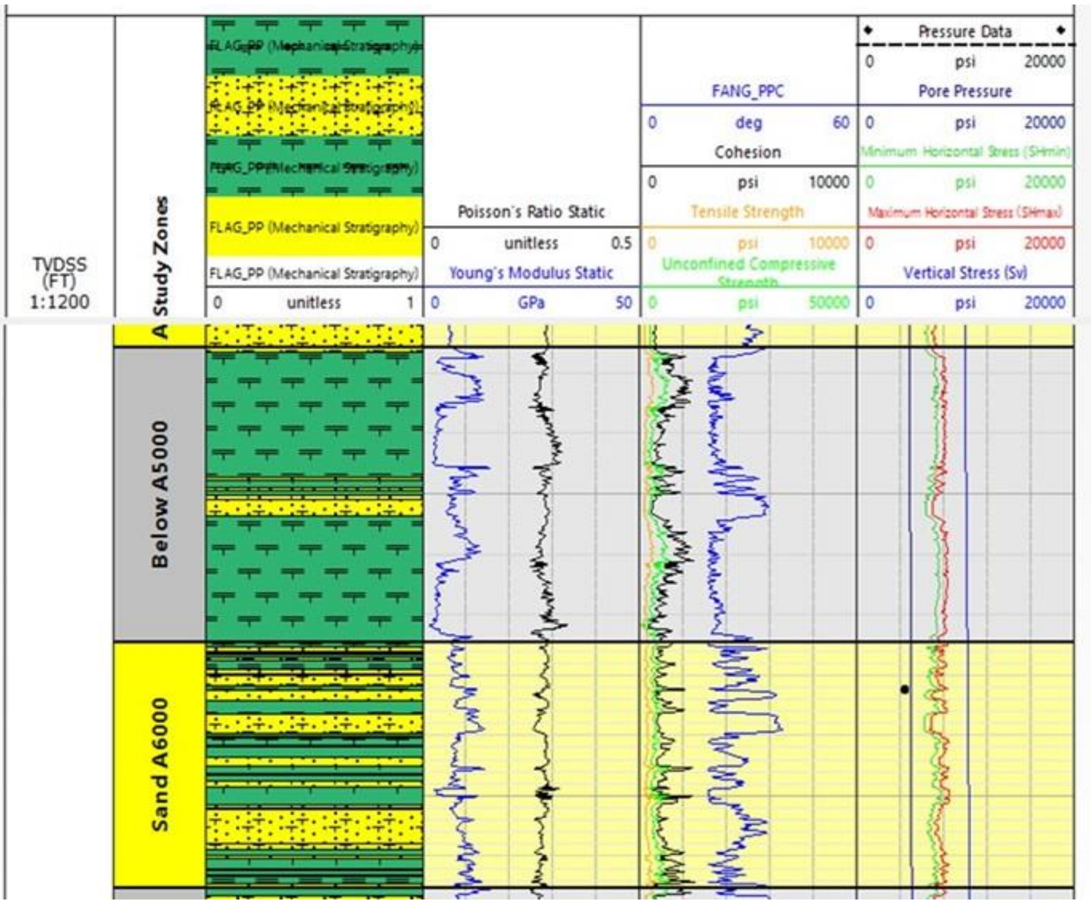

Fig. 10. 1D MEM of well TOBA-05 for zone below A5000 and Sand A6000

The geomechanical results (1D MEM result) presented for Well TOBA-05 in Table 3 above and Fig. 9 and 10 offers valuable insight into the stress and strength properties of both caprock and reservoir formations across three key intervals: below 9200 ft (caprock), the A3000 saline formation (9200–9311 ft), and the deeper units comprising the A5000 caprock (10840–11078 ft) and A6000 hydrocarbon reservoir (11085–11280 ft). These values are essential for assessing the structural stability and containment capacity of geological formations targeted for CO_2 sequestration.

In the caprock interval below 9200 ft, the average Young's Modulus (YM) is 4.95 GPa, indicating moderate rock stiffness. The Poisson's Ratio (PR) remains relatively stable at 0.31, reflecting a balanced elastic response. The friction angle (FANG) averages 24.58°, while cohesion (COH) is 665.91 psi and the Unconfined Compressive Strength (UCS) is 2427.71 psi, showing the caprock is mechanically competent but less robust than deeper units. The pore pressure (P_P) at this depth averages 3592.86 psi. In terms of stress, the total minimum horizontal stress (σh) is 5727.00 psi, maximum horizontal stress (σH) is 6299.71 psi, and vertical stress (σv) is 8177.43 psi. The corresponding effective stresses which are critical for evaluating fracture risk are 2314.14 psi (σh), 2706.86 psi (σH), and 4544.57 psi (σv).

In the A3000 reservoir, mechanical properties remain similar. The YM is 4.91 GPa, PR is again 0.31, while FANG (frictional angle) slightly increases to 26.61°. Cohesion averages 631.89 psi and UCS is 2064.75 psi, slightly lower than the overlying caprock. Pore pressure rises to 4156.50 psi, and the total stresses are 5803.00 psi (σh), 6383.50 psi (σH), and 8425.50 psi (σv). The corresponding effective stresses are 1646.50 psi, 2227.00 psi, and 4269.00 psi, suggesting moderate effective stress conditions, still within a safe operational window for CO_2 injection.

Table 3. Numerical values of elastic properties, rock strength properties and stress profile of TOBA

TOBA-05	**DEPTH (ft)**	**PR**	**YM (Gpa)**	**FANG (deg)**	**COH (psi)**	**TS (psi)**	**UCS (psi)**	**PP (psi)**	**TOTAL σh (psi)**	**TOTAL σH (psi)**	**TOTAL σV (psi)**	**EFF (σh) (psi)**	**EFF (σH) (psi)**	**EFF (σV) (psi)**
BELOW A2OOO (CAPROCK)	8770.00	0.31	4.18	25.00	530.00	167.40	4167.00	3946.00	5564.00	6120.00	7976.00	1618.00	2174.00	4030.00
	8800.00	0.29	6.06	33.60	588.00	218.20	2182.00	3960.00	5137.00	5650.00	8006.00	1177.00	1690.00	4046.00
	8850.00	0.30	2.86	30.22	453.00	157.90	1579.00	982.00	5327.00	5860.00	8054.00	4345.00	4878.00	7072.00
	8900.00	0.32	8.49	22.70	674.37	202.80	2028.00	4005.00	5816.00	6398.00	8100.00	1811.00	2393.00	4095.00
	9000.00	0.31	5.89	24.65	724.72	226.00	2260.00	4050.00	5755.00	6331.00	8197.00	1705.00	2281.00	4147.00
	9100.00	0.34	2.17	19.00	659.29	184.85	1848.00	4095.00	6231.00	6854.00	8297.00	2136.00	2759.00	4202.00
	9138.00	0.31	4.97	19.00	1032.00	289.50	2895.00	4112.00	6259.00	6885.00	8332.00	2147.00	2773.00	4220.00
AVERAGE	**8936.86**	**0.31**	**4.95**	**24.88**	**665.91**	**206.66**	**2422.71**	**3592.86**	**5727.00**	**6299.71**	**8137.43**	**2134.14**	**2706.86**	**4544.57**
SAND A30000 (RESERVOIR)	9140.00	0.29	4.35	25.00	753.39	236.5	2365.00	4113.00	5825.00	6408.00	8334.00	1712.00	2295.00	4221.00
	9200.00	0.29	7.34	33.43	607.60	225.88	2258.00	4140.00	5370.00	5907.00	8390.00	1230.00	1767.00	4250.00
	9300.00	0.30	5.33	29.00	590.40	200.61	2006.00	4184.00	5678.00	6245.00	8484.00	1494.00	2061.00	4300.00
	9311.00	0.33	2.66	22.00	576.20	163.06	1630.00	4189.00	6339.00	6974.00	8494.00	2150.00	2785.00	4305.00
AVERAGE	**9237.75**	**0.31**	**4.91**	**26.6075**	**631.89**	**206.51**	**2064.75**	**4156.50**	**5803.00**	**6383.50**	**8425.50**	**1646.50**	**2227.00**	**4269.00**
BELOW A5OOO (CAPROCK)	10840.00	0.28	8.659	32.5	774.9	282.63.00	2826.00	4878.00	6413.00	7054.00	9981.00	1535.00	2176.00	5103.00
	10900.00	0.29	2.984	20.97	793.12	230.6.00	2306.00	4905.00	7334.00	8067.00	10041.00	2429.00	3162.00	5136.00
	11000.00	0.269	11.46	20.20	1986.00	569.62	5693.00	4985.00	7474.00	8221.00	10138.00	2489.00	3236.00	5153.00
	11078.00	0.289	6.885	27.00	851.00	278.08	2781.00	4986.00	6946.00	7640.00	10211.00	1960.00	2654.00	5225.00
AVERAGE	**10954.50**	**0.282**	**7.497**	**25.17**	**1101.255**	**340.23**	**3401.50**	**4938.50**	**7041.75**	**7745.50**	**10092.75**	**2103.25**	**2807.00**	**5154.25**
SAND A60000 (RESERVOIR)	11085.00	0.27	8.50	32.00	865.50	315.40	3154.00	4989.00	6563.00	7219.00	10217.00	1574.00	2230.00	5228.00
	11100.00	0.29	8.50	21.00	1347.00	393.30	3933.00	4995.00	7454.00	8200.00	10233.00	2459.00	3205.00	5238.00
	11200.00	0.29	7.78	27.50	918.20	302.78	3028.00	5040.00	7986.00	7684.90	10330.00	2946.00	2644.90	5290.00
	11280.00	0.26	12.25	19.70	2138.50	608.30	6033.00	5076.00	7712.00	8484.00	10409.00	2636.00	3408.00	5333.00
AVERAGE	**11166.25**	**0.27**	**9.27**	**25.05**	**1317.30**	**404.95**	**4037.00**	**5025.00**	**7428.75**	**7896.98**	**10297.25**	**2403.75**	**2871.97**	**5272.25**

Moving deeper to the caprock below 10840 ft (A5000 interval), rock mechanical strength significantly increases. YM averages 7.50 GPa, and FANG is 25.17°, while cohesion rises markedly to 1101.26 psi, and UCS to 3401.50 psi, indicating a stronger and more brittle lithology. Pore pressure is higher at 4938.50 psi, with total stresses also elevated: 7041.75 psi (σh), 7745.50 psi (σH), and 10092.75 psi (σv). Effective stresses at this depth rise to 3103.25 psi, 2807.00 psi, and 5154.25 psi respectively suggesting improved rock sealing ability and lower leakage risk compared to shallower units.

In the deeper hydrocarbon reservoir A6000 interval, the rock demonstrates the highest mechanical competence. YM reaches 9.27 GPa, the highest across all intervals, with FANG at 25.05°, cohesion at 1317.30 psi, and UCS peaking at 4037.00 psi. These values imply an extremely strong and stiff formation. Pore pressure increases to 5025.00 psi, while total stresses further rise to 7428.75 psi (σh), 7896.98 psi (σH), and 10297.25 psi (σv). The effective stresses here are the highest: 2403.75 psi (σh), 2871.97 psi (σH), and 5272.25 psi (σv). These stress conditions indicate that the formation is geomechanically stable, less likely to undergo fault slip or fracturing under injection pressures, and therefore presents the most secure zone for CO_2 sequestration. According to Fjaer et al. (2008) the value of Young's static modulus in shale is around 0.1 - 1.0 Mpsi (0.5–7 Gpa) and sandstone is about 2 - 10 Mpsi (14–68 Gpa). Poisson's ratio (0.1–0.25) means rocks fracture easier whereas high Poisson's ratio (0.35–0.45) indicates the rocks are harder to fracture. Gercek (2007) gave range for the Poisson ratio in some rocks, which shows that shale is in the range 0.05 - 0.32, sandstone is in the range 0.05 - 0.4, and limestone is in the range 0.1 - 0.32. The frictional angle average value of the caprocks of the caprock of saline and hydrocarbon reservoir correspond with low frictional angle suggested by Barton & Choubey (1977) and Wyllie & Norrish (2017) The progressive increase in mechanical strength and effective stress with depth in Well TOBA-05 suggests a strong, brittle lithology favourable for long-term CO_2 storage, with the A6000 reservoir standing out as the most competent unit both in terms of geomechanical resilience and containment integrity.

Also The 1D Mechanical Earth Model (MEM) analysis carried out on well TOBA-05, as shown in Fig.s 9 and 10 and summarized in Table 3, reveals key insights into the in-situ stress regime of the study area. The data indicate that the effective vertical stress (σv) consistently exhibits the highest magnitude across the evaluated depth intervals, followed by the effective maximum horizontal stress (σH), while the effective minimum horizontal stress (σh) remains the lowest.

According to Anderson's faulting theory (1951), such a stress distribution where Sv > σH > σh is indicative of a **normal faulting regime**. This aligns with the tectonic setting where the overburden acts as the maximum principal stress, and extensional forces dominate.

Furthermore, this normal faulting environment is suggestive of **growth faults**, which are a common feature in deltaic sedimentary basins like the Niger Delta. As described by Auduson (2018), growth faults are synsedimentary normal faults characterized by vertical displacements that increase with depth. Their association with the Niger Delta supports the interpretation that the TOBA field is structurally influenced by such fault systems, which have important implications for reservoir compartmentalization, seal integrity, and CO_2 storage potential.

3.5 Skerlec's Model for Brittleness and ductility

Table 4 below presents the average density and depth of the shale caprock associated with both saline formation and hydrocarbon reservoirs across four wells (TOBA-04 to TOBA-07). These density values were used in plotting the Skerlec's model (Fig. 11) to assess the brittleness or ductility of the formations. The ductility of the caprocks

(Shale) using Skerlec's model in (1982) divided into 3 major zones in consonance with Hoshino et al (1972) and Boggs (1995) include;

(a) Ductile Zone (< 2.2 g/cm³): Shales with densities below 2.2 g/cm³ are ductile, meaning they deform plastically under stress without fracturing. This behaviour is typical of shallow-depth mudrocks with minimal compaction and cementation, such as shales at low burial stress.

(b) Transitional Zone (2.2–2.5 g/cm³): Shales in this density range exhibit both brittle and ductile behavior depending on local factors (e.g., stress state, mineral composition and pore pressure). This zone marks the depth where compaction, cementation, and diagenesis begin to significantly influence rock mechanical properties.

(c) Brittle Zone (> 2.5 g/cm³): Shales with densities above 2.5 g/cm³ are brittle, prone to fracturing under stress. Typically found at deeper burial depths, these shales undergo compaction and diagenesis, which reduce porosity and increase rock strength.

In TOBA-04, no density value is recorded for the saline formation due to the absence of density logs in shallower depth intervals for this well. However, the hydrocarbon reservoir has a density of 2.4228 g/cm³ at 3596.47 m, consistent with dense, deeper reservoir rocks. For TOBA-05, both formations are represented: the saline formation has a density of 2.2760 g/cm³ at 2785.95 m, while the hydrocarbon zone is lower in density (2.1877 g/cm³ at 3374.75 m), possibly indicating more porous or gas-bearing lithology in the hydrocarbon zone. In TOBA-06, the density increases with depth, as expected. The saline formation has 2.2545 g/cm³ at 2795.02 m, and the deeper hydrocarbon zone has 2.3456 g/cm³ at 3310.31 m, reflecting compaction and lithological differences. TOBA-07 displays a similar trend: 2.3318 g/cm³ (saline at 3120.09 m) and 2.4238 g/cm³ (hydrocarbon at 3894.62 m), again affirming the trend of increasing density with depth and lithological maturity. These subtle density increases in the hydrocarbon zones suggest greater compaction, which often results in reduced porosity and increased stiffness. The absence of density measurements in the saline formation is not due to poor-quality data but rather due to the limited depth coverage of the density log.

Table 4. Average density of shale and depth of caprock (shale) of saline formation and reservoir of interest

WELL TOBA-05	**DENSITY (g/cm³)**	**DEPTH (m)**
SALINE (A3000)	2.2760	2785.9482
HYDROCARBON (A6000)	2.1877	3374.7456
WELL TOBA-04	**DENSITY(g/cm³)**	**DEPTH (m)**
SALINE (A3000)	________	________
HYDROCARBON (A6000)	2.4228	3596.4693
WELL TOBA-07	**DENSITY(g/cm³)**	**DEPTH (m)**
SALINE (A3000)	2.3318	3120.0852
HYDROCARBON (A6000)	2.4238	3894.6201
WELL TOBA-06	**DENSITY(g/cm³)**	**DEPTH (m)**
SALINE (A3000)	2.2545	2795.0160
HYDROCARBON (A6000)	2.34561	3310.3058

The Skerlec's model in the Fig. 11 below shows that the caprocks with higher densities (above ~2.35 g/cm³) tend to cluster on the brittle to very brittle side of the curve. These are mostly hydrocarbon reservoir caprocks (represented in red), implying that the higher compaction and mineral content at these depths enhance their brittleness. In contrast, the saline formation caprocks (yellow) are positioned closer to the ductile–brittle boundary, associated with slightly lower densities and shallower depths, indicating less compaction and more deformable behaviour.

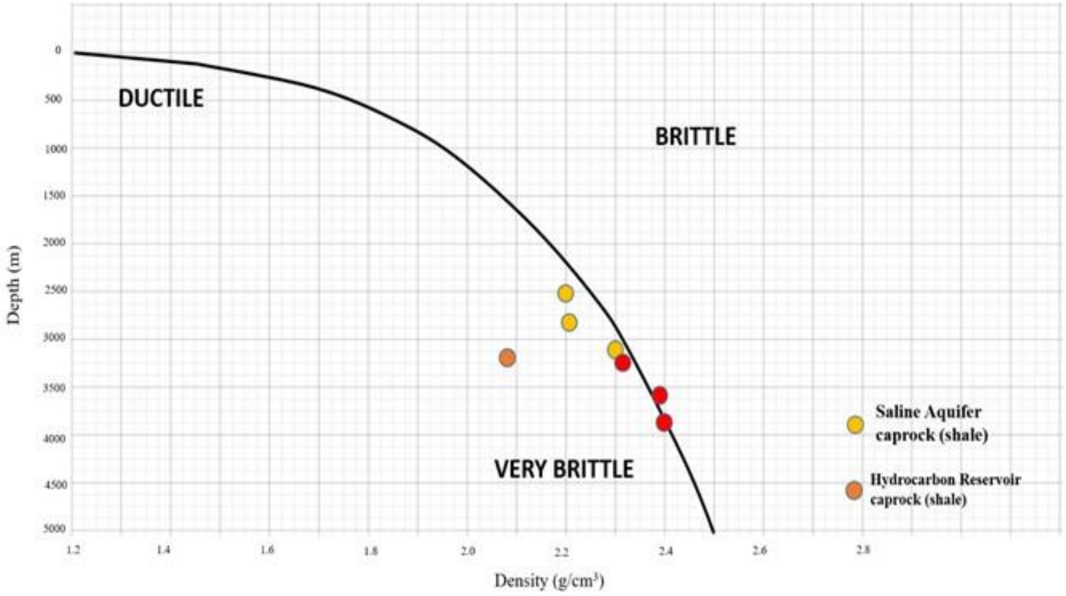

Fig. 11. Plot of depth (m) against density (g/cm^3) to determine ductility and brittleness of caprocks

Higher shale density, as seen in hydrocarbon zones, correlates with increased compaction and thus more brittle behaviour. Conversely, lower density saline formation shales tend to remain more ductile due to lesser burial depth and compaction. This brittleness-ductility behavior captured in the Skerlec's model is crucial for assessing caprock integrity and reservoir seal efficiency.

3.6 Brittleness Index (Young's Modulus and Poisson Ratio)

Brittleness as a characteristic of broken or broken material with little or no plastic flow (Holt et al., 2011). Brittle rocks have no characteristics of ductility and plasticity and break straight after the loss of a stress-strain relationship. The transition of ductility to brittleness depends upon the magnitude of the stress applied to the material.

As a result of the lack of right definition or concept, measurement of brittleness has not been standardized. Grieser and Bray (2007), expressed the term average brittleness as an empirical relationship between Poisson's ratio and Young's modulus to distinguish ductile from the brittle area.

The brittleness index was conducted using Young's Modulus and Poisson Ratio. The result is shown below in Table 5.The brittleness index analysis, based on the classification criteria by Rojas et al. (2016) and June & Yang et al. (2013) in Table 6 below, offers valuable insight into the mechanical behaviour of formations relevant for CO_2 storage. In analyzing the brittleness index derived from Poisson's ratio and Young's modulus, distinct mechanical characteristics emerge across the formations and caprocks in well TOBA-05. The caprock of the saline formation exhibits a Young's modulus of 0.174021 and a Poisson's ratio of 0.372198, resulting in a brittleness index of 0.27311. This value places it in the less ductile category, indicating it is relatively soft and more prone to plastic deformation rather than fracturing. Similarly, the saline reservoir shows a Young's modulus of 0.173062 and Poisson's ratio of 0.385791, with a brittleness index of 0.279426, also classifying it as less ductile. These two saline units both caprock and reservoir therefore exhibit ductile behaviour, with a lower tendency to fracture under stress.

Table 5. Brittleness average of TOBA-05 for both saline formation and hydrocarbon reservoir

WELL	Formation Type	Lithology	YM (E)	PR (ν)	AVERAGE
TOBA-05	Saline formation	CAPROCK (Shale)	0.174021	0.372198	0.273110
TOBA-05	Hydrocarbon reservoir	CAPROCK (Shale)	0.263774	0.433877	0.348825
TOBA-05	Saline formation	RESERVOIR (Sandstone)	0.173062	0.385791	0.279426
TOBA-05	Hydrocarbon reservoir	RESERVOIR (Sandstone)	0.326091	0.448712	0.387401

Table 6. Relationship between brittleness index and brittleness of rock modified from (from Rojas et al., 2016 and Yang et al., 2013)

Brittleness index	Nature of rock in terms of brittleness
0-0.16	Ductile
0.16-0.32	Less ductile
0.32-0.48	Less brittle
Greater than 0.48	Brittle

In contrast, the hydrocarbon caprock has a higher Young's modulus of 0.263774 and a Poisson's ratio of 0.433877, yielding a brittleness index of 0.348825. This value falls in the less brittle category, suggesting that the hydrocarbon caprock is moderately brittle, stiffer than the saline rocks but not fully brittle. The most mechanically brittle unit is the hydrocarbon reservoir, which records the highest Young's modulus of 0.326091 and Poisson's ratio of 0.448712, leading to a brittleness index of 0.387401. This value places it near the upper end of the "less brittle" range, indicating a clear tendency toward brittle behaviour.

The saline formation caprock and reservoir are ductile, the hydrocarbon caprock is moderately brittle, and the hydrocarbon reservoir is the most brittle of all the units analysed. This variation in brittleness has important implications for geomechanical stability under CO_2 injection. The brittle nature of the hydrocarbon reservoir makes it more susceptible to fracturing and tensile failure, while the ductile behaviour of the saline units means they are more likely to deform by shear under stress. Understanding these mechanical differences is essential for predicting how each unit may respond during CO_2 storage operations and ensuring seal integrity is maintained.

Reservoir rocks that fall into the less brittle range, as seen in the hydrocarbon-bearing formation, could be more amenable to controlled fracturing, which can enhance injectivity without compromising containment. Conversely, the less ductile saline reservoir may require more conservative injection strategies to avoid undesirable deformation or seal damage.

The absence of extreme brittleness or ductility in any of the formations is advantageous. Highly brittle rocks could fracture uncontrollably, while highly ductile rocks may deform excessively, closing pore spaces. The transitional mechanical properties observed here are ideal for CO_2 storage, providing both containment security and structural stability.

3.7 Stress Analysis for Fault (3D Mohr Circle)

Fault stability analysis in this study is based on evaluating slip tendency and dilation tendency, which quantify the likelihood of fault reactivation and fracture opening, respectively, under the current in-situ stress regime. By examining these parameters, this analysis identifies fault segments that may become critically stressed during injection operations and assesses their potential impact on seal integrity and storage performance in the TOBA-05 field. Structural containment of CO_2 relies on low-permeability caprock and fault stability (Sun et al., 2023). Fig. 12 to Fig. 15 below shows the state of stress of faults in well TOBA-05.

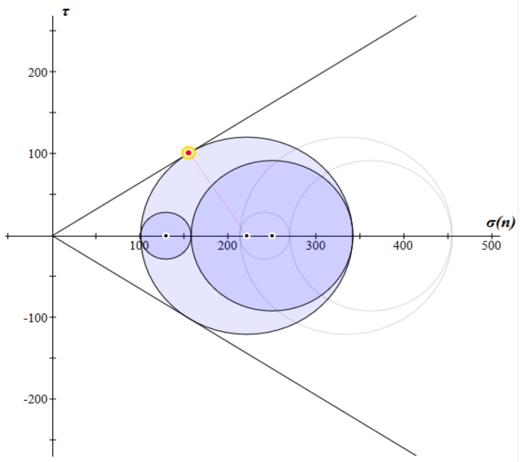

Initial Condition (σ1 = 454.6, σ2 = 270.7, σ3 = 213.4)$*10^1$psi
$\tau = 101.07*10^1$psi
σn = $268.25*10^1$psi
$T_s = 0.38$
📫Pp causing failure = $112.75*10^1$psi/7.78Mpa
At Failure (σ1 = 341.44, σ2 = 157.88, σ3 = 99.86) $*10^1$psi
$\tau = 101.00*10^1$psi
σn = $152.53*10^1$psi
$T_s = 0.66$

Fig. 12. Mohr plot of TOBA-05 Saline Formation Caprock (fault)

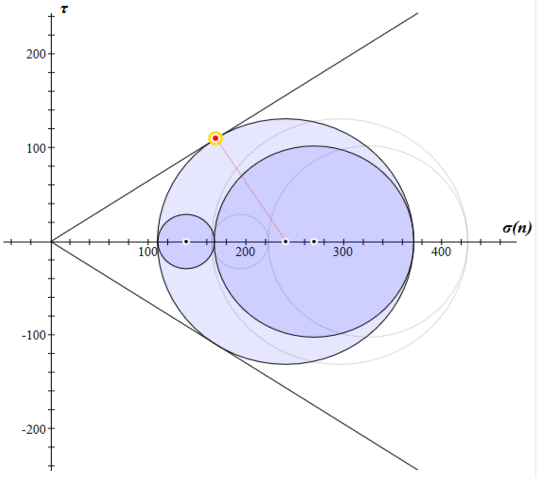

Initial Condition (σ1 = 426.9, σ2 = 222.7, σ3 = 164.7) $*10^1$psi
$\tau = 109.92*10^1$psi
σn = $224.35*10^1$psi
$T_s = 0.48$
📫Pp causing failure = $55.24*10^1$psi/3.80Mpa
At Failure (σ1 = 371.82, σ2 = 169.56, σ3 = 108.52) $*10^1$psi
$\tau = 110.72*10^1$psi
σn =$168.56*10^1$psi
$T_s = 0.65$

Fig. 13. Mohr plot of TOBA-05 Saline Formation Sandstone (fault)

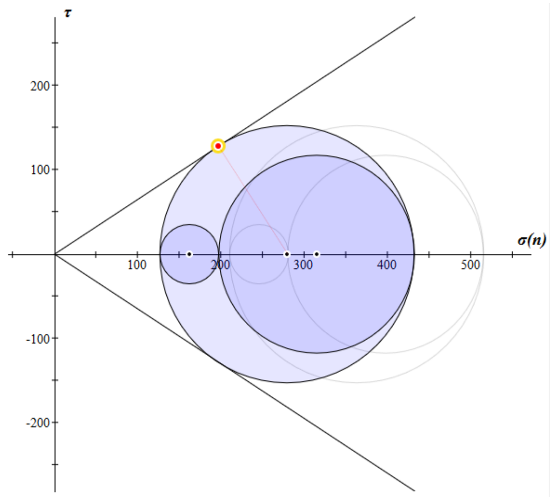

Initial Condition (σ1 = 515.4, σ2 = 280.7, σ3 = 210.3) *10^1psi
τ = 127.90*10^1psi
σn = 279.71*10^1psi
T_s = 0.45
Pp causing failure = 82.94*10^1psi/5.72Mpa
At Failure (σ1 = 432.65, σ2 = 198.06, σ3 = 126.27) *10^1psi
τ = 130.01*10^1psi

Fig. 14. Mohr plot of TOBA-05 Hydrocarbon Reservoir Caprock (fault)

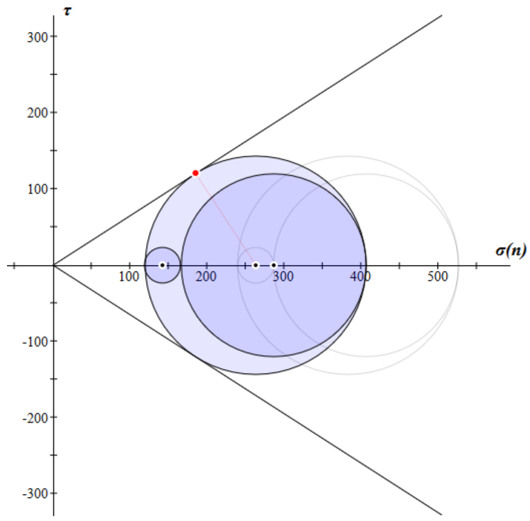

Initial Condition (σ1 = 527.2, σ2 = 287.2, σ3 = 240.4) *10^1psi
τ = 120.23*10^1psi
σn = 305.65*10^1psi
T_s = 0.39
Pp causing failure = 120.60*10^1psi/8.32Mpa
At Failure (σ1 = 407.30, σ2 = 166.30, σ3 = 119.30) *10^1psi
τ = 122.36*10^1psi
σn = 184.85*10^1psi

Fig. 15. Mohr plot of TOBA-05 Hydrocarbon Reservoir (fault)

The Mohr circle analyses for the TOBA-05 fault provide crucial insights into the mechanical behaviour of faults under CO_2 injection scenarios, focusing on caprock and reservoir intervals of both saline formations and hydrocarbon-bearing units. Each Mohr plot captures the evolution from the fault's initial in-situ stress condition (faint circles) to the failure state (bold blue circles), highlighting the pore pressure increment required to bring the fault to critical conditions.

In the saline formation caprock shown in Fig. 12, the initial stress conditions are σ_1 = 4546 psi, σ_2 = 2707 psi, and σ_3 = 2134 psi, with an effective shear stress (τ) of 1010.7 psi and normal stress (σn) of 2682.5 psi, giving a slip tendency (Ts) of 0.38 that is well below the slip threshold. However, when the pore pressure increases by 1127 psi (7.78 MPa), the fault transitions to a reactivated state, with reduced principal stresses of σ_1 = 3414.4 psi, σ_2 = 1578.8 psi, and σ_3 = 999.6 psi. At this point, τ remains nearly constant (1010.0 psi), but σn drops to 1525.3 psi, and the slip tendency increases to Ts = 0.66, exceeding the critical slip threshold of 0.6 defined by

Cotesta et al. (2007), indicating fault failure and potential breach of the seal.

For the saline reservoir sandstone in Fig. 13, the stress values suggest this unit is the most vulnerable. Initial stresses are σ_1 = 4269 psi, σ_2 = 2227 psi, and σ_3 = 1647 psi, with τ = 1099.2 psi, σn = 2243.5 psi, and Ts = 0.48. Failure is induced by a modest increase in pore pressure of 552.4 psi (3.80 MPa), reducing the stress state to σ_1 = 3718.2 psi, σ_2 = 1695.6 psi, and σ_3 = 1085.2 psi. The corresponding τ = 1107.2 psi and σn = 1685.6 psi result in a slip tendency of Ts = 0.65, again surpassing the failure threshold. Notably, this pressure threshold (3.80 MPa) is comparable to the value reported by Umar et al. (2020), who concluded that in their study area, a fault requires at least 3.2 MPa of additional pore pressure to fail. This similarity underscores a shared geomechanical stability between both study areas and supports the TOBA field's suitability for CO_2 sequestration, provided that the injection pressures are carefully managed.

The hydrocarbon reservoir caprock seen in Fig. 14 exhibits greater mechanical stability, with initial stresses of σ_1 = 5154 psi, σ_2 = 2807 psi, and σ_3 = 2103 psi. The initial τ = 1279 psi and σn = 2797.1 psi result in a Ts = 0.45. Fault slip only occurs when the pore pressure increases by 829.4 psi (5.72 MPa), reducing the stress regime to σ_1 = 4326.5 psi, σ_2 = 1980.6 psi, and σ_3 = 1262.7 psi. At failure, τ = 1300.1 psi and σn = 1981.1 psi yield a Ts = 0.66, again exceeding the critical slip tendency.

The hydrocarbon reservoir sandstone displayed in Fig. 15 is the most mechanically robust of all units evaluated. Its initial stress state is σ_1 = 5272 psi, σ_2 = 2872 psi, and σ_3 = 2404 psi, with τ = 1202.3 psi and σn = 3056.5 psi, resulting in Ts = 0.39. Fault reactivation in this unit requires a pore pressure increase of 1206 psi (8.32 MPa) which is the highest among all examined intervals. At failure, the new stresses are σ_1 = 4073 psi, σ_2 = 1663 psi, and σ_3 = 1193 psi, with τ = 1223.6 psi and σn = 1848.5 psi, resulting in a Ts = 0.66. This confirms that the unit maintains stability under elevated pressure and is ideal for safe CO_2 injection.

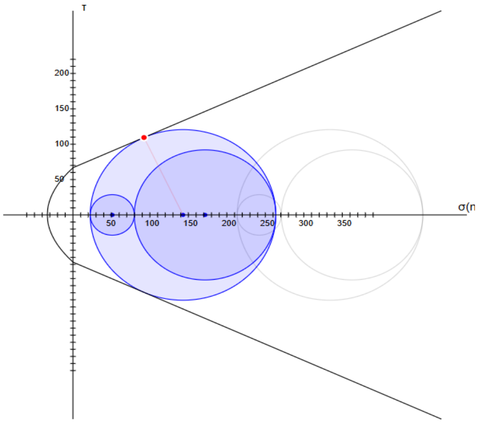

Initial Condition ($\sigma1 = 454.6$, $\sigma2 = 270.7$, $\sigma3 = 213.4)*10^1$psi
τ = 109.41*101psi
σn = 283.26*101psi
Ts = 0.386
📪Pp causing failure =190.96*10^1psi/13Mpa
At Failure ($\sigma1$=263.40, $\sigma2$=80.31, $\sigma3$=21.98) *101psi
τ = 109.95*101psi

Fig. 16. Mohr plot of TOBA-05 Saline Caprock Formation (intact rock)

The quantitative stress analysis across TOBA-05 faults shows varying degrees of fault stability, with hydrocarbon reservoir formations offering the greatest resistance to slip and saline formations especially the sandstone reservoir more prone to fault reactivation. The critical slip tendency threshold of 0.6, as proposed by Cotesta et al. (2007), serves as a reliable indicator of failure across all units. According to Streit et al. (2005), to avoid damage to top seal and fault seals due to injection-related pore pressure increase, maximum sustainable pore pressures need to be estimated for CO_2 injection. The minimum reactivation pressure (3.80 MPa) aligns closely with Umar et al.

(2020)’s 3.2 MPa benchmark, reinforcing the mechanical credibility of the TOBA field as a candidate for long-term CO_2 storage, while also highlighting the need for targeted monitoring and pressure control strategies, particularly in more vulnerable saline intervals.

3.7 Stress Analysis for Intact Rock (3D Mohr Circle)

The mechanical strength and failure behaviour of intact rocks both reservoir and caprock are essential factors influencing the feasibility of long-term CO_2 storage. This analysis employs 3D Mohr circle plots to evaluate the stress states and failure envelopes of key formations in the TOBA-05 well, allowing for a detailed understanding of how these rocks respond to increasing pore pressure. Key parameters such as principal stresses, shear and normal stresses, slip tendency, and pore pressure at failure are used to characterize the rocks' stability. Combined with brittleness index classification, this assessment provides insight into each formation's ability to maintain structural integrity and containment under CO_2 injection conditions.

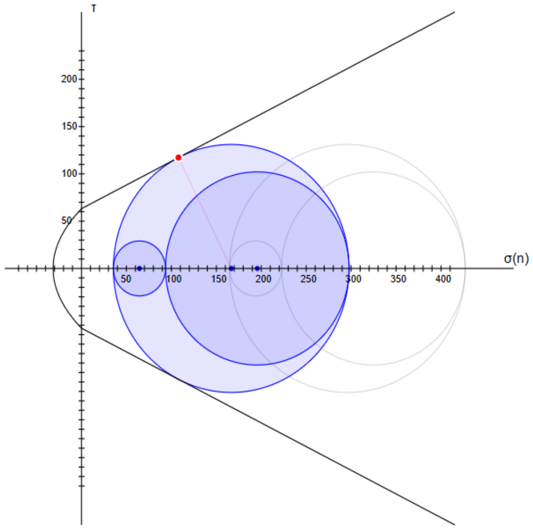

Initial Condition (σ1 = 426.9, σ2 = 222.7, σ3 = 164.7) *10^{1}psi
τ = 117.22*10^{1}psi
σn = 237.10*10^{1}psi
T_s = 0.49
📫Pp causing failure = 129.22*10^{1}psi/8.91Mpa
At Failure (σ1=298.35, σ2=93.04, σ3=35.11) *10^{1}psi
τ = 118.39*10^{1}psi
σn = 107.25*10^{1}psi
T_s = 0.91

Fig. 17. Mohr plot of TOBA-05 Saline Formation Sandstone (intact rock)

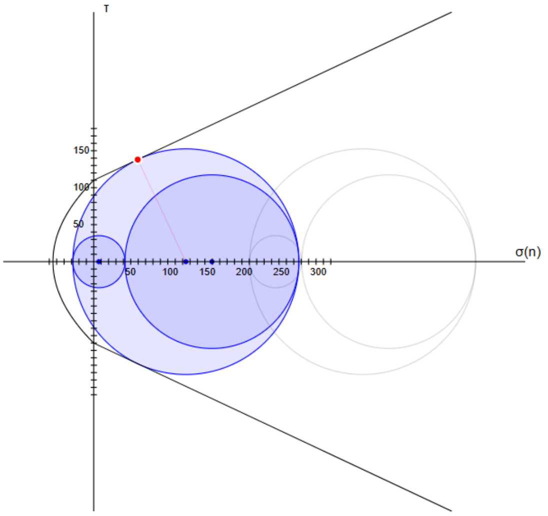

Initial Condition (σ1 = 515.4, σ2 = 280.7, σ3 = 210.3) *10^{1}psi
τ = 138.03*10^{1}psi
σn = 297.90*10^{1}psi
T_s = 0.46
📫Pp causing failure = 238.54*10^{1}psi/16.50Mpa
At Failure (σ1 = 277.73, σ2 = 42.44, σ3 = -28.57) *10^{1}psi
τ = 140.60*10^{1}psi
σn = 58.77*10^{1}psi
T_s = 2.4

Fig. 18. Mohr plot of TOBA-05 Hydrocarbon Reservoir Caprock (intact rock)

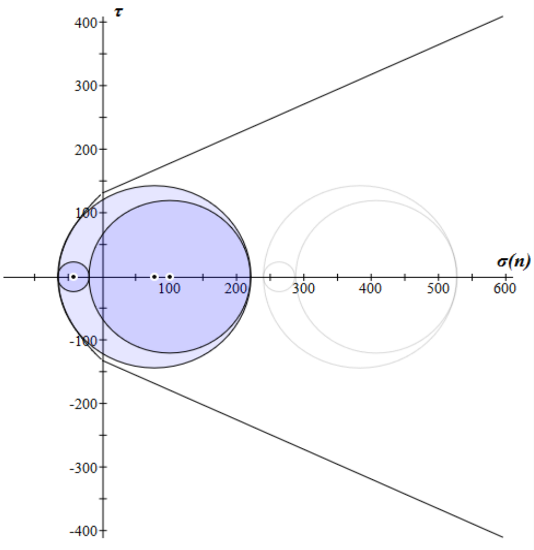

Initial Condition ($\sigma1 = 527.2$, $\sigma2 = 287.2$, $\sigma3 = 240.4$) *10^1psi
$\tau = 202.80$*10^1psi
$\sigma n = 767.60$*10^1psi
$T_s = 0.49$
ΔPp causing failure = 306.00*10^1psi/21.10Mpa
At Failure ($\sigma1 = 222.04$, $\sigma2 = -19.61$, $\sigma3 = -65.85$) *10^1psi
$\sigma_3 \geq$ Tensile strength (-65.85*10^1psi)

Fig. 19. Mohr plot of TOBA-05 Hydrocarbon Reservoir (intact rock)

The 3D Mohr circle analysis conducted on the intact rock samples from the TOBA-05 well offers a detailed view of the mechanical behaviour of subsurface formations under varying stress conditions, particularly in the context of CO_2 injection. These Mohr plots capture two key states for each lithological unit: the initial effective stress condition (represented by faint circles) and the stress condition at failure (depicted by bold blue circles). This approach enables a clear visualization of the stress response of each formation to changes in pore pressure, allowing for the identification of failure modes and critical thresholds that may be encountered during CO_2 storage operations.

According to Nygård et al. (2006), brittle failure typically occurs in stiff lithologies with high shear strength, leading to sudden fracturing, while ductile failure is characterised by more diffuse deformation throughout the rock mass without the formation of distinct fracture planes (Rutter et al., 1986; Jaeger et al., 2009). These theoretical principles are reflected in the progressive failure behaviour observed across the four lithological units evaluated in TOBA-05.

In the case of the saline formation caprock (Fig. 16), the rock is initially subjected to high principal stresses ($\sigma_1 = 4546$ psi, $\sigma_2 = 2707$ psi, $\sigma_3 = 2134$ psi), with a corresponding shear stress (τ) of 1094.1 psi and a normal stress (σ_n) of 2832.6 psi. The initial slip tendency (Ts) of 0.386 suggests stable conditions, well below the 0.6 critical threshold for slip. At failure, despite a slight increase in shear stress ($\tau = 1099.5$ psi) and a reduced $\sigma_n = 915.4$ psi, Ts only rises to 0.83, and failure is achieved under a significant pore pressure increment (ΔPp) of 1909.6 psi (13 MPa). The rock's mechanical stability under high stress and its moderate brittleness index of 0.27311 ("less ductile") confirm its integrity and effectiveness as a reliable seal for CO_2 containment.

The saline formation sandstone reservoir (Fig. 17) exhibits slightly lower initial stresses ($\sigma_1 = 4269$ psi, $\sigma_3 = 1647$ psi) and a Ts of 0.49. At failure, Ts increases to 0.91 and dilation tendency (Td) to 0.64, with a ΔPp of 1292.2 psi (8.91 MPa) required for failure. This indicates a higher risk of fracture dilation and fault reactivation under injection pressure. With a brittleness index of 0.279426, also classified as "less ductile," this unit maintains moderate stiffness but is more vulnerable than the caprock above it. While this reservoir could support CO_2 injection due to its injectivity, careful monitoring and pressure management would be necessary to maintain seal integrity.

In contrast, the hydrocarbon reservoir caprock (Fig. 18) displays more pronounced stress changes. The initial stress state includes $\sigma_1 = 5154$ psi and $\sigma_3 = 2103$ psi, with an initial

Ts of 0.46. At failure, Ts spikes dramatically to 2.4 well above the 0.6 threshold while normal stress drops significantly to 587.7 psi, and ΔPp reaches 2385.4 psi (16.5 MPa). This behaviour suggests a high likelihood of brittle shear failure or fault slip. The caprock's brittleness index of 0.348825 ("less brittle") implies some stiffness, but the high Ts value at failure highlights its susceptibility to mechanical compromise under elevated pressures. This caprock may require additional verification of stability before being relied upon for long-term CO_2 containment.

Finally, the hydrocarbon reservoir rock (Fig. 19) presents the most critical behaviour. It has the highest initial stresses (σ_1 = 5272 psi, σ_3 = 2404 psi) and a Ts of 0.49. Upon failure, the minimum principal stress (σ_3) becomes tensile (–658.5 psi), exceeding the rock's tensile strength and resulting in pure tensile failure. The ΔPp needed to trigger this failure is 3060 psi (21.10 MPa) the highest of all formations studied. Tensile failure is especially concerning, as it can initiate vertical fractures that compromise CO_2 containment. The rock's brittleness index of 0.387401, the highest among all formations, indicates it is the most brittle unit and highly prone to fracturing. While this enhances its potential for injectivity, it demands robust caprock integrity to prevent leakage.

Collectively, the 3D Mohr circle analysis demonstrates a clear transition in failure mode and deformation style across the formations from ductile shear failure in the saline caprock to brittle tensile failure in the hydrocarbon reservoir. This transition reflects an increasing tendency toward brittle behaviour, corroborated by the rising brittleness index values. These observations are consistent with the theoretical models of Nygård et al. (2006) and Jaeger et al. (2009), which link lithological stiffness and brittleness to failure mechanism.

In terms of pressure tolerance, the hydrocarbon reservoir withstands the highest pore pressure before failure (21.10 MPa), followed by the hydrocarbon caprock (16.5 MPa), the saline caprock (13 MPa), and the saline reservoir (8.91 MPa). However, a higher pressure threshold does not necessarily imply superior containment, especially when the failure mode is tensile, as seen in the hydrocarbon reservoir. From a CO_2 storage perspective, the most mechanically favourable injection scenario involves targeting the saline reservoir, underlain by the robust saline caprock. This combination offers optimal conditions of moderate brittleness, lower slip tendency, and mechanical resilience for both injectivity and secure containment. In contrast, while the hydrocarbon reservoir may offer improved injectivity due to its brittleness, its use for long-term CO_2 storage must be carefully evaluated, ensuring that an effective caprock barrier is in place.

The integration of Mohr failure envelope analysis with brittleness profiling presents a robust framework for evaluating the geomechanical suitability of subsurface formations for CO_2 sequestration. The mechanical properties observed across the TOBA-05 well characterized by transitional, non-extreme brittleness and stress resilience support both containment integrity and injection feasibility, provided that operational pressures remain within safe limits.

4.0 Conclusion

This research fills a vital knowledge gap in carbon storage safety by quantitatively evaluating the brittleness, ductility, and failure behaviour of caprock and reservoir formations in the TOBA field, Niger Delta elements often neglected in prior assessments. The ability to distinguish between brittle and ductile mechanical responses under injection-induced stress is essential, as it governs the risk of leakage, containment integrity, and long-term CO_2 storage performance under supercritical conditions. The results demonstrate a clear trend of depth dependent mechanical strengthening, with Young's Modulus increasing by 87% and UCS by 66% from the shallow caprock to the deeper A6000 reservoir. Skerlec's classification and BI values reveal a mechanical spectrum from ductile saline formations (BI = 0.27) to brittle hydrocarbon-bearing zones (BI = 0.39), with failure mechanisms transitioning from shear to tensile modes. The A6000 reservoir, exhibiting the highest pore pressure resilience and tensile strength, emerges as the most secure storage candidate. Conversely, saline formations are more susceptible to fault reactivation and require stricter pressure control ($\Delta Pp < 3.80$ MPa). The prevailing normal faulting regime ($Sv > \sigma H > \sigma h$), verified through stress analysis, aligns with the tectonic setting of the Niger Delta and supports the likelihood of growth faulting. By bridging the gap in understanding how subsurface formations respond mechanically to injection, this study delivers a validated, physics-based framework for risk mitigation, operational planning, and long-term storage assurance in geological carbon sequestration projects.

5.0 References

Abiola, O., & Obasuyi, F. O. (2020). Transition zones analysis using empirical capillary pressure model from well logs and 3D seismic data on ‘Stephs’ field, onshore, Niger Delta, Nigeria. *Journal of Petroleum Exploration and Production Technology, 10, 4,* pp. 1227–1242.

Aird, P. (2019). Deepwater Geology & Geoscience. *Deepwater Drilling, 17-68.*

Albukhari, T. M., Beshish, G. K., Abouzbeda, M. M., & Madi, A. B. D. A. S. A. L. A. M. (2018, March). Geomechanical wellbore stability analysis for the reservoir section in JNC186 oil field. In ISRM 1st International Conference on Advances in Rock Mechanics-TuniRock (pp. ISRM-TUNIROCK-2018-22). International Society for Rock Mechanics and Rock Engineering (ISRM).

Anderson, E. M. (1951). *The dynamics of faulting and dyke formation with applications to Britain* (2nd ed.). Oliver and Boyd.

Archer, S., & Rasouli, V. (2012). A log based analysis to estimate mechanical properties and in-situ stresses in a shale gas well in North Perth Basin. *Petroleum and Mineral Resources, 21*, pp. 122–135.

Auduson, A. E. (2018). *Concise Applied Geophysics: A Practical Approach*. Delizon Publishers.

Avbovbo, A. A. (1978). Geothermal gradients in the Southern Nigerian basin. *Bulletin of Canadian Petroleum Geology, 26, 2*, pp. 268–274.

Avbovbo, A. A. (1978). Tertiary lithostratigraphy of Niger delta. *AAPG Bulletin, 62, 2*, pp. 295–300.

Barros, C., & Andrade, A. (2009, August). Well Correlation by Fuzzy Inference. In *11th International Congress of the Brazilian Geophysical Society* (pp. cp-195). European Association of Geoscientists & Engineers.

Barton, N., & Choubey, V. (1977). The shear strength of rock joints in theory and practice. *Rock mechanics, 10*, pp. 1–54.

Biot, M. A., & Willis, D. G. (1957). The elastic coefficients of the theory of consolidation. *Journal of Applied Mechanics, 24*, pp. 594–601.

Boggs, S., Jr. (1995). *Principles of sedimentology and stratigraphy* (2nd ed.). Prentice Hall.

Boot-Handford, M. E., Abanades, J. C., Anthony, E. J., Blunt, M. J., Brandani, S., Mac Dowell, N., & Fennell, P. S. (2014). Carbon capture and storage update. *Energy & Environmental Science, 7, 1,* pp. 130–189.

Bowers, G. L. (1995). Pore pressure estimation from velocity data: Accounting for overpressure mechanisms besides undercompaction. *SPE Drilling & Completion, 10, 2*, pp. 89–95.

Bui, M., Adjiman, C. S., Bardow, A., Anthony, E. J., Boston, A., Brown, S., ... & Mac Dowell, N. (2018). Carbon capture and storage (CCS): the way forward. *Energy & Environmental Science, 11, 5*, pp. 1062–1176.

Byerlee, J. (1978). Friction of rocks. *Rock friction and earthquake prediction*, pp. 615–626.

Cao, X., Wang, H., Yang, K., Wu, S., Chen, Q., and Bian, J. (2022, December). Hydrate-based CO2 sequestration technology: Feasibilities, mechanisms, influencing factors, and applications. Journal of Petroleum Science and Engineering, 219, 111121. https://doi.org/10.1016/j.petrol.2022.111121.

Castagna, J. P., Batzle, M. L., Kan, T. K., & Backus, M. M. (1993). Rock physics—The link between rock properties and AVO response. *Offset-dependent reflectivity—Theory and practice of AVO analysis: SEG*, *8*, pp. 135-171.

Castagna, J.P., Bazle, M.L., and Eastwood, R.L. (1985). "Relationships Between Compressional Wave and Shear Wave Velocities in Clastic Silicates". *Geophysica*, *50*, *4*, pp. 571–581.

Cerveny, K., Davies, R., Dudley, G., Kaufman, P., Knipe, R. J., & Krantz, B. (2004). Reducing uncertainty with fault-seal analysis. *Oilfield Review*, *16*, *4*, pp. 38–51.

Climate Watch. (2019). Climate Watch - Data for Climate Action.

Cotesta, L., Kaiser, P. K., Cai, M., & Vorauer, A. (2007). Application of scientific visualisation-Stress control on permeability anisotropy in moderately fractured rock. In *ARMA Canada-US Rock Mechanics Symposium* (pp. ARMA-07). ARMA.

Doust, H., Omatsola, M. (1990). Petroleum geology of the Niger delta. *Geological Society, London, Special Publications*, *50*, pp. 365–365.

Eigbe, P. A., Ajayi, O. O., Olakoyejo, O. T., Fadipe, O. L., Efe, S., & Adelaja, A. O. (2023). A general review of CO_2 sequestration in underground geological formations and assessment of depleted hydrocarbon reservoirs in the Niger Delta. *Applied Energy*, *350*, 121723. https://doi.org/10.1016/j.apenergy.2023.121723

Ekweozor, C. M., & Okoye, N. V. (1980). Petroleum Source-Bed Evaluation of Tertiary Niger Delta: GEOLOGIC NOTES. *AAPG Bulletin*, *64*, *8*, pp. 1251–1259.

Ferrill, D. A. (1999). Stressed rock strains groundwater at Yucca Mountain, Nevada. *GSA Today*, *9*, *5*, pp. 1–8.

Ferrill, D. A., Smart, K. J., & Morris, A. P. (2020). Fault failure modes, deformation mechanisms, dilation tendency, slip tendency, and conduits v. seals. *Geological Society, London, Special Publications*, *496*, *1*, pp. 75–98.

Fjaer, E., Holt, R. M., Horsrud, P., Raaen, A. M., & Risnes, R. (2008). *Petroleum related rock mechanics 2nd edition*.

Folorunso, A. F., Li, Y., & Liu, Y. (2015). Characteristics of marine CSEM responses in complex geologic terrain of Niger Delta Oil province: Insight from 2.5 D finite element forward modeling. *Journal of African Earth Sciences*, *102*, pp. 18–32.

Gercek, H. (2007). Poisson's ratio values for rocks. *International Journal of Rock Mechanics and Mining Sciences*, *44*, *1*, pp. 1–13.

Grieser, B., & Bray, J. (2007, March). Identification of production potential in unconventional reservoirs. In *SPE Oklahoma City Oil and Gas Symposium/Production and Operations Symposium* (pp. SPE-106623). SPE.

Hajdarwish, A. M. (2006). *Geologic controls of shear strength behavior of mudrocks*. (Doctoral dissertation).

Holt, R. M., Fjaer, E., Nes, O. M., & Alassi, H. T. (2011, June). A shaly look at brittleness. In *ARMA US Rock Mechanics/Geomechanics Symposium* (pp. ARMA-11). ARMA.

Hoshino, K., Koide, H., Inami, K., Iwamura, S., & Mitsui, S. (1972). *Mechanical properties of Japanese Tertiary sedimentary rocks under high confining pressures* (Report No. 5676). Geological Survey of Japan.

Ighalo, J. O., Dulta, K., Kurniawan, S. B., Omoarukhe, F. O., Ewuzie, U., Eshiemogie, S. O., Ojo, A. U., and Abdullah, S. R. S. (2022, September). Progress in Microalgae Application for CO2 Sequestration. Cleaner Chemical Engineering, 3, 100044. https://doi.org/10.1016/j.clce.2022.100044

Ingram, G. M., & Urai, J. L. (1999). Top-seal leakage through faults and fractures: the role of mudrock properties. *Geological Society, London, Special Publications, 158, 1*, pp. 125–135.

Jaeger, J. C., Cook, N. G. W., & Zimmerman, R. (2009). *Fundamentals of rock mechanics*.

Jolly, R. J. H., & Sanderson, D. J. (1997). A Mohr circle construction for the opening of a pre-existing fracture. *Journal of Structural Geology, 19, 6*, pp. 887–892.

Kadyrov, T., & Tutuncu, A. N. (2012). Integrated wellbore stability analysis for well trajectory optimization and field development in the West Kazakhstan Field. In *ARMA US Rock Mechanics/Geomechanics Symposium*. ARMA.

Knöll, L. O. (2016). *The process of building a mechanical earth model using well data* [Master's thesis, Montanuniversität Leoben].

Kulikowski, D., Amrouch, K., & Cooke, D. (2016). Geomechanical modelling of fault reactivation in the Cooper Basin, Australia. *Australian Journal of Earth Sciences, 63, 3*, pp. 295–314.

Labuz, J. F., & Zang, A. (2014). Mohr–Coulomb failure criterion. *The ISRM Suggested Methods for Rock Characterization, Testing and Monitoring: 2007-2014*, pp. 227–231.

Lee, D. H., Liao, C. J., Wu, J. H., Huang, Y. F., & Luo, G. L. (2017). A procedure for determining the preliminary maximum injection pressure for CO2 sequestration. *Terr. Atmos. Ocean. Sci., 28*, pp. 217–228.

Legentil, C., Pellerin, J., Raguenel, M., & Caumon, G. (2023). Towards a workflow to evaluate geological layering uncertainty on CO2 injection simulation. *Applied Computing and Geosciences, 18*, pp. 100118.

Mavko, G., Mukerji, T., & Dvorkin, J. (2020). *The rock physics handbook* (3rd ed.). Cambridge University Press. https://books.google.com.ng/books?id=FMS-DwAAQBAJ

McKeagney, C. J., Boulter, C. A., Jolly, R. J. H., & Foster, R. P. (2004). 3-D Mohr circle analysis of vein opening, Indarama lode-gold deposit, Zimbabwe: implications for exploration. *Journal of Structural Geology, 26, 6-7*, pp. 1275–1291.

Metz, B., Davidson, O., De Coninck, H. C., Loos, M., & Meyer, L. (2005). *IPCC special report on carbon dioxide capture and storage*.

Mildren, S. D., Hillis, R. R., Dewhurst, D. N., Lyon, P. J., Meyer, J. J., & Boult, P. J. (2005). FAST: A new technique for geomechanical assessment of the risk of reactivation-related breach of fault seals. In P. Boult & J. Kaldi (Eds.), *Evaluating fault and cap rock seals* (pp. 73-85). American Association of Petroleum Geologists.

Moeck, I., Kwiatek, G., & Zimmermann, G. (2009). Slip tendency analysis, fault reactivation potential and induced seismicity in a deep geothermal reservoir. *Journal of Structural Geology, 31, 10*, pp. 1174–1182.

Mutadza, I., Ikiensikimama, S. S., & Joel, O. F. (2024). Geo-mechanical and geo-morphology characterisation of the cap rocks in the Niger Delta for potential carbon capture and storage. *Heliyon, 10*(10),e31206. https://doi.org/10.1016/j.heliyon.2024.e31206

Nacht, P. K., de Oliveira, M. F., Roehl, D. M., & Costa, A. M. (2010). Investigation of geological fault reactivation and opening. *Mecánica computacional, 29, 89*, pp. 8687–8697.

Nwachukwu, J. I., & Chukwura, P. I. (1986). Organic matter of Agbada Formation, Niger Delta, Nigeria. *AAPG bulletin, 70, 1*, pp. 48–55.

Nygård, R., Gutierrez, M., Bratli, R. K., & Høeg, K. (2006). Brittle–ductile transition, shear failure and leakage in shales and mudrocks. *Marine and Petroleum Geology, 23, 2*, pp. 201–212.

Obasuyi, F. O., Abiola, O., Egbokhare, O. J., Ifanegan, A. S., & Ekere, J. I. (2019). 3D seismic and structural analysis of Middle Agbada reservoir sand, Offshore Niger Delta, Nigeria. *Journal of Geography, Environment and Earth Science International, 20, 3, pp.* 1–10. https://doi.org/10.9734/JGEESI/2019/v20i330108

Ogagarue, D. O. (2008). Localized Vp-Vs relationships for the Niger delta sediments. *Pacific Journal of Science and Technology, 9, 2*, pp. 558–561.

Osokpor, J., & Maju-Oyovwikowhe, E. G. (2021). Paleodepositional Environment and Sequence Stratigraphy of Miocene Sediments in Well TN-1, Coastal Swamp Depobelt, Niger Delta Basin, Nigeria. *Tanzania Journal of Science, 47, 5*, pp. 1530–1545.

Pan, P., Wu, Z., Feng, X., & Yan, F. (2016). Geomechanical modeling of CO2 geological storage: A review. *Journal of Rock Mechanics and Geotechnical Engineering, 8, 6*, pp. 936–947.

Raziperchikolaee, S., & Pasumarti, A. (2020). The impact of the depth-dependence of in-situ stresses on the effectiveness of stacked caprock reservoir systems for CO2 storage. *Journal of Natural Gas Science and Engineering*, *79*, pp. 103361.

Rojas, L. F., Peña, Y. Q., & Carrillo, Z. H. (2016, June). Brittleness analysis: A methodology to identify sweet spots in shale gas reservoirs. In *SPE Argentina Exploration and Production of Unconventional Resources Symposium* (p. D011S003R001). SPE.

Rutqvist, J., Birkholzer, J., Cappa, F., & Tsang, C. F. (2007). Estimating maximum sustainable injection pressure during geological sequestration of CO2 using coupled fluid flow and geomechanical fault-slip analysis. *Energy Conversion and Management, 48, 6*, pp. 1798–1807.

Rutter, E. H., Maddock, R. H., Hall, S. H., & White, S. H. (1986). Comparative microstructures of natural and experimentally produced clay-bearing fault gouges. *Pure and applied geophysics*, *124*, pp. 3–30.

Short, K. C., & Stäuble, A. J. (1967). Outline of geology of Niger Delta. *AAPG bulletin, 51, 5*, pp. 761–779.

Sibson, R. H. (1990). Conditions for fault-valve behaviour. *Geological Society, London, Special Publications, 54, 1*, pp. 15–28.

Sibson, R.H. (1985). A note on fault reactivation. *J. Struct. Geol, 7*, pp. 751–754.

Sibson, R.H. (2000). A brittle failure mode plot defining conditions for high-flux flow. *Econ. Geol, 95, 1*, pp. 41–48.

Słota-Valim, M. (2015). Static and dynamic elastic properties, the cause of the difference and conversion methods–case study. *Nafta-Gaz*, *11*, pp. 816–826.

Song, Y., Jun, S., Na, Y., Kim, K., Jang, Y., & Wang, J. (2023). Geomechanical challenges during geological CO2 storage: A review. *Chemical Engineering Journal*, *456*, pp. 140968.

Streit, J. E., & Hillis, R. R. (2002, October). Estimating fluid pressures that can induce reservoir failure during hydrocarbon depletion. In *SPE/ISRM Rock Mechanics Conference* (pp. SPE-78226). SPE

Streit, J. E., & Hillis, R. R. (2004). Estimating fault stability and sustainable fluid pressures for underground storage of CO2 in porous rock. *Energy*, *29, 9-10*, pp. 1445–1456.

Sun, Z., Salazar-Tio, R., Wu, L., Bostrøm, B., Fager, A., & Crouse, B. (2023). Geomechanical assessment of a large-scale CO2 storage and insights from uncertainty analysis. *Geoenergy Science and Engineering*, *224*, pp. 211596.

Sundquist, E., Burruss, R., Faulkner, S., Gleason, R., Harden, J., Kharaka, Y., Tieszen, L., & Waldrop, M. (2008). Carbon sequestration to mitigate climate change. Fact Sheet. https://doi.org/10.3133/fs20083097

Twiss, R. J., & Moores, E. M. (1992). *Structural geology* (Illustrated, reprint ed.). W. H. Freeman

Umar, B. A., Gholami, R., Nayak, P., Shah, A. A., & Adamu, H. (2020). Regional and field assessments of potentials for geological storage of CO₂: A case study of the Niger Delta Basin, Nigeria. *Journal of Natural Gas Science and Engineering, 77*, 103195. https://doi.org/10.1016/j.jngse.2020.103195.

Whiteman, A. (1982). *Nigeria: Its petroleum geology, resources and potential: Volume 1*. Springer Dordrecht. https://doi.org/10.1007/978-94-009-7361-9

Wyllie, D. C. (2017). Rock strength properties and their measurement. In *Rock slope engineering* (pp. 117-162). CRC Press.

Yang, Y., Sone, H., Hows, A., & Zoback, M. D. (2013, June). Comparison of brittleness indices in organic-rich shale formations. In *ARMA US Rock Mechanics/Geomechanics Symposium* (pp. ARMA-2013). ARMA.

Yin, Z. M., & Ranalli, G. (1992). Critical stress difference, fault orientation and slip direction in anisotropic rocks under non-Andersonian stress systems. *Journal of Structural Geology, 14, 2*, pp. 237–244.

Zoback, M. D. (2007). *Reservoir geomechanics*. Cambridge University Press. https://doi.org/10.1017/CBO9780511586477

Zoback, M. D. (2010). *Reservoir geomechanics* (Illustrated, reprint ed.). Cambridge University Press.

Compliance with Ethical Standards

Declarations

The authors declare that they have no conflict of interest.

Data availability

All data used in this study will be readily available to the public

Availability of data and materials

The publisher has the right to make the data public.

Competing interests

The authors declared no conflict of interest.

Funding

The authors declared no source of funding.

Authors' contributions

Olowonefa Richard conceptualized the study, coordinated data acquisition, and supervised the analysis. Auduson Aaron Enechojo conducted geomechanical modelling, stress regime evaluation, and result interpretation. Ologe Oluwatoyin processed and analyzed geophysical datasets. Yusuf Odunsanwo contributed industry insights, field data, and interpretation validation. Agbane Isaac Ojodomo assisted in literature review, data processing, and manuscript preparation.